The Astrophysical Journal, 962:95 (28pp), 2024 February 10 https://doi.org/10.3847/1538-4357/ad1033

CLASSY. VIII. Exploring the Source of Ionization with UV Interstellar Medium Diagnostics in Local High-z Analogs*

Matilde Mingozzi[1,2], Bethan L. James[2], Danielle A. Berg[3], Karla Z. Arellano-Córdova[4], Adele Plat[5], Claudia Scarlata[6], Alessandra Aloisi[1], Ricardo O. Amorín[7,8], Jarle Brinchmann[9], Stéphane Charlot[10], John Chisholm[3], Anna Feltre[11], Simon Gazagnes[3], Matthew Hayes[12], Timothy Heckman[13], Svea Hernandez[2], Lisa J. Kewley[14,15], Nimisha Kumari[2], Claus Leitherer[1], Crystal L. Martin[16], Michael Maseda[17], Themiya Nanayakkara[18], Swara Ravindranath[19], Jane R. Rigby[19], Peter Senchyna[20], Evan D. Skillman[6], Yuma Sugahara[21,22,23], Stephen M. Wilkins[24], Aida Wofford[25], and Xinfeng Xu[26,27]
[1] Space Telescope Science Institute, 3700 San Martin Drive, Baltimore, MD 21218, USA; mmingozzi@stsci.edu
[2] AURA for ESA, Space Telescope Science Institute, 3700 San Martin Drive, Baltimore, MD 21218, USA
[3] Department of Astronomy, The University of Texas at Austin, 2515 Speedway, Stop C1400, Austin, TX 78712, USA
[4] Institute for Astronomy, University of Edinburgh, Royal Observatory, Edinburgh, EH9 3HJ, UK
[5] Institute for Physics, Laboratory for Galaxy Evolution, EPFL, Observatoire de Sauverny, Chemin Pegasi 51, 1290 Versoix, Switzerland
[6] Minnesota Institute for Astrophysics, University of Minnesota, 116 Church Street SE, Minneapolis, MN 55455, USA
[7] ARAID Foundation. Centro de Estudios de Física del Cosmos de Aragón (CEFCA), Unidad Asociada al CSIC, Plaza San Juan 1, E–44001 Teruel, Spain
[8] Departamento de Astronomía, Universidad de La Serena, Avenida Juan Cisternas 1200 Norte, La Serena 1720236, Chile
[9] Instituto de Astrofísica e Ciências do Espaço, Universidade do Porto, CAUP, Rua das Estrelas, PT4150-762 Porto, Portugal
[10] Sorbonne Université, CNRS, UMR7095, Institut d'Astrophysique de Paris, F-75014, Paris, France
[11] INAF—Osservatorio Astrofisico di Arcetri, Largo E. Fermi 5, I-50157 Firenze, Italy
[12] Stockholm University, Department of Astronomy and Oskar Klein Centre for Cosmoparticle Physics, AlbaNova University Centre, SE-10691, Stockholm, Sweden
[13] Center for Astrophysical Sciences, Department of Physics & Astronomy, Johns Hopkins University, Baltimore, MD 21218, USA
[14] Research School of Astronomy and Astrophysics, Australian National University, Cotter Road, Weston Creek, ACT 2611, Australia
[15] ARC Centre of Excellence for All Sky Astrophysics in 3 Dimensions (ASTRO 3D), Canberra, ACT 2611, Australia
[16] Department of Physics, University of California, Santa Barbara, Santa Barbara, CA 93106, USA
[17] Department of Astronomy, University of Wisconsin-Madison, 475 North Charter Street, Madison, WI 53706 USA
[18] Swinburne University of Technology, Melbourne, Victoria, Australia
[19] Observational Cosmology Lab, Code 665, NASA Goddard Space Flight Center, 8800 Greenbelt Road, Greenbelt, MD 20771, USA
[20] Carnegie Observatories, 813 Santa Barbara Street, Pasadena, CA 91101, USA
[21] Institute for Cosmic Ray Research, The University of Tokyo, Kashiwa-no-ha, Kashiwa 277-8582, Japan
[22] National Astronomical Observatory of Japan, 2-21-1 Osawa, Mitaka, Tokyo 181-8588, Japan
[23] Waseda Research Institute for Science and Engineering, Faculty of Science and Engineering, Waseda University, 3-4-1, Okubo, Shinjuku, Tokyo 169-8555, Japan
[24] Astronomy Centre, University of Sussex, Falmer, Brighton BN1 9QH, UK
[25] Instituto de Astronomía, Universidad Nacional Autónoma de México, Unidad Académica en Ensenada, Km 103 Carr. Tijuana-Ensenada, Ensenada 22860, México
[26] Department of Physics and Astronomy, Northwestern University, 2145 Sheridan Road, Evanston, IL 60208, USA
[27] Center for Interdisciplinary Exploration and Research in Astrophysics (CIERA), Northwestern University, 1800 Sherman Avenue, Evanston, IL 60201, USA
Received 2023 June 21; revised 2023 November 21; accepted 2023 November 24; published 2024 February 9

Abstract

In the current JWST era, rest-frame UV spectra play a crucial role in enhancing our understanding of the interstellar medium (ISM) and stellar properties of the first galaxies in the epoch of reionization ($z > 6$). Here, we compare well-known and reliable optical diagrams sensitive to the main ionization source (i.e., star formation, SF; active galactic nuclei, AGN; and shocks) to UV counterparts proposed in the literature—the so-called "UV–BPT diagrams"—using the HST COS Legacy Archive Spectroscopic SurveY (CLASSY), which is the largest high-quality, high-resolution, and broad-wavelength range atlas of far-UV spectra for 45 local star-forming galaxies. In particular, we explore where CLASSY UV line ratios are located in the different UV diagnostic plots, taking into account state-of-the-art photoionization and shock models, and, for the first time, the measured ISM and stellar properties (e.g., gas-phase metallicity, ionization parameter, carbon abundance, and stellar age). We find that the combination of C III] $\lambda\lambda$1907,9 He II λ1640 and O III] λ1666 can be a powerful tool to separate between SF, shocks, and AGN at subsolar metallicities. We also confirm that alternative diagrams without O III] λ1666 still allow us to define an SF-locus, with some caveats. Diagrams including C IV $\lambda\lambda$1548,51 should be taken with caution given the complexity of this doublet profile. Finally, we present a discussion detailing the ISM conditions required to detect UV emission lines, visible only in low gas-phase metallicity ($12 + \log(\mathrm{O/H}) \lesssim 8.3$) and high ionization parameter ($\log(U) \gtrsim -2.5$) environments. Overall, CLASSY and our UV toolkit will be crucial in interpreting the spectra of the earliest galaxies that JWST is currently revealing.

* Based on observations made with the NASA/ESA Hubble Space Telescope, obtained from the Data Archive at the Space Telescope Science Institute, which is operated by the Association of Universities for Research in Astronomy, Inc., under NASA contract NAS 5-26555.

Unified Astronomy Thesaurus concepts: Dwarf galaxies (416); Ultraviolet astronomy (1736); Galaxy chemical evolution (580); Galaxy spectroscopy (2171); High-redshift galaxies (734); Emission line galaxies (459)

1. Introduction

Emission lines provide precious information about the conditions and ionizing sources of the interstellar medium (ISM) in galaxies across cosmic time. Several classification methods have been proposed to identify the main ionization sources: hot and young massive stars, tracing recent star formation (SF); post–asymptotic giant branch (post-AGB) stars, tracing older stellar populations; active galactic nuclei (AGN), and thus the energy of the accretion disk surrounding a central supermassive black hole; low-ionization (nuclear) emission-line regions (LI(N)ERs); shocks, due to supernovae and stellar winds, outflows from starbursts/AGN activity and mergers, or from random motions of interstellar clouds; accretion on compact objects (e.g., high-nass x-ray binaries, HMXB); or a mixture of them (e.g., Heckman 1980; Izotov & Thuan 1999; Kewley et al. 2006; Nagao et al. 2006; Allen et al. 2008; Stasińska et al. 2015; Belfiore et al. 2016).

Historically, the main diagnostics to discriminate between different ISM ionization mechanisms are the classical optical-diagnostic diagrams, which were first presented in Baldwin et al. (1981) (and usually referred as BPT diagrams) and then progressively updated by Keel (1983), Veilleux & Osterbrock (1987), Kauffmann et al. (2003), and Kewley et al. (2006). These diagrams are constructed on intensity ratios of strong emission lines close in wavelength, namely [N II] λ6584/Hα, [S II] $\lambda\lambda$6717,31/Hα and [O I] λ6300/Hα versus [O III] λ5007/Hβ (i.e., [N II], [S II] and [O I] BPT diagrams), minimizing the effects of differential reddening by dust and flux calibration issues. They have been found useful to discriminate between H II-like sources and objects photoionized by a harder radiation field (e.g., power-law continuum by an AGN or shock excitation). However, existing BPT diagrams can be less effective in discriminating mechanisms other than SF in metal-poor galaxies (e.g., Groves et al. 2006; Reines et al. 2020; Polimera et al. 2022), since, on the one hand, the involved line ratios can be dependent on metallicity and, on the other hand, the hot metal-poor stellar populations have a hard spectrum to irradiate the gas (e.g., Feltre et al. 2016; Byler et al. 2018; Xiao et al. 2018; Wofford et al. 2021). In addition, these diagnostics are not optimal in discriminating shocks from other ionization sources.

Exploiting the large statistics of the Sloan Digital Sky Survey's Data Release 7 (SDSS DR7; Abazajian et al. 2009), Shirazi & Brinchmann (2012) proposed a less metallicity-dependent diagnostic diagram to discriminate the ionization source: [N II]/Hα versus He II λ4686/Hβ. He II λ4686 is produced via recombination and thus indicates the existence of sources of hard ionizing radiation capable of ionizing the helium (ionization potential of 54.4 eV). Such a high radiation field can be produced not only by young stellar populations (massive and very massive stars), including O-type stars (e.g., Sixtos et al. 2023) and some types of Wolf–Rayet (WR) stars (e.g., WC, WO, and WNE, Schaerer & Vacca 1998; see also Schmutz et al. 1992), but also other mechanisms such as AGN (Shirazi & Brinchmann 2012), X-ray binaries (Garnett et al. 1991; Mayya et al. 2023), or shocks (Dopita & Sutherland 1996; Thuan & Izotov 2005; Stasińska et al. 2015; Alarie & Morisset 2019) can play a role. Recently, Tozzi et al. (2023) investigated the Shirazi & Brinchmann (2012) diagnostic diagram with integral-field spectroscopy (IFS) observations from the SDSS-IV MaNGA (Mapping Nearby Galaxies at APO; Bundy et al. 2015) survey, confirming its power in revealing AGN activity undetected from the classical BPT diagrams. Finally, to better disentangle the presence of shocks, Kewley et al. (2019) presented an overview of alternative optical diagrams, including [O III] λ5007, [O II] λ3727, and [O I] λ6300 emission lines (see also Heckman 1980; Allen et al. 2008), as well as the importance of correlations between line ratios and the velocity dispersion of the gas. Overall, the combination of (some of) these optical criteria provides a reliable powerful tool to investigate the ISM ionization sources in galaxies.

However, the well-studied optical emission lines (from [O II] $\lambda\lambda$3727 to [S III] $\lambda\lambda$9069, 9532) on which the diagnostics described in the previous paragraphs rely are not easily accessible to investigate the early phases of galaxy evolution in the epoch of reionization (EoR; $z > 6$) in the current JWST and future extremely large ground-based telescopes (ELTs) era. For example, JWST/NIRspec does not cover Hα at $z \gtrsim 6.5$ and [O III] $\lambda\lambda$4959,5007 at $z \gtrsim 10$ anymore, while JWST/MIRI is less sensitive and does not have multi-object slit capabilities. Hence, rest-frame UV emission lines have started to play a critical role in understanding EoR objects, which makes a reliable UV toolkit of ISM diagnostics essential. EoR galaxies are expected to be increasingly compact, metal-poor, with low-masses and large specific star formation rates (SFRs; e.g., Wise et al. 2014; Madau & Haardt 2015; Robertson et al. 2015; Stanway et al. 2016; Stark 2016), and characterized by prominent high-ionization nebular UV emission lines (e.g., He II λ1640, O III] $\lambda\lambda$1661, 6, C III] $\lambda\lambda$1907,9, C IV $\lambda\lambda$1548,51; Stark et al. 2015; Mainali et al. 2017, 2018). The spectra of some of these objects have already started to be revealed with JWST/NIRSpec (e.g., Arellano-Córdova et al. 2022a; Curti et al. 2022; Matthee et al. 2023; Arrabal Haro et al. 2023; Curtis-Lake et al. 2023; Trump et al. 2023), with one of the furthest ($z \sim 10.603$) galaxies ever spectroscopically observed characterized by plenty of UV (from Lyα to Mg II $\lambda\lambda$2795, 2802) and optical (from [O II] $\lambda\lambda$3727 to [O III] λ4363) emission lines (Bunker et al. 2023b). In the foreseeable future, further JWST observations including large surveys such as GLASS (e.g., Castellano et al. 2022; Roberts-Borsani et al. 2022; Treu et al. 2022), CEERS (e.g., Finkelstein et al. 2022; Arrabal Haro et al. 2023), and JADES (e.g., Bunker et al. 2023b; Curtis-Lake et al. 2023) will provide more rest-frame UV spectra of $z > 6$ systems, exploring the EoR in depth.

Several recent works proposed UV alternatives to the optical diagnostics, either using photoionization models from SF and AGN (Feltre et al. 2016; Jaskot & Ravindranath 2016; Dors et al. 2018; Nakajima et al. 2018; Byler et al. 2020) and shock models (Jaskot & Ravindranath 2016), or from a comparison of either models and simulations (Hirschmann et al. 2019, 2023). For instance, F16 proposed various UV diagnostic plots, including the C III] $\lambda\lambda$1907,9/He II λ1640 versus C IV $\lambda\lambda$1548,51/He II λ1640 to discriminate between SF and AGN models (see also Dors et al. 2018). Jaskot & Ravindranath (2016) used the same diagnostic diagram to separate SF from shocks models, while Nakajima et al. (2018) proposed alternative models and diagrams based on C IV $\lambda\lambda$1548,51/C III] $\lambda\lambda$1907,9 and their equivalent widths (EWs). Finally, Hirschmann et al. (2019, 2023) coupled

models and cosmological zoom-in simulations, exploring synthetic optical and UV emission-line diagnostic diagrams, listing the most promising in Table 1 of Hirschmann et al. (2023). However, UV diagnostics have yet to be compared against the optical ones in a systematic way because it is not trivial to observe a full suite of optical and UV lines capable of probing the different ISM properties (e.g., density, temperature, metallicity, ionization parameter), which is fundamental for interpreting the results.

The analysis of local galaxies can provide the tools to interpret high-z galaxies, given the high signal-to-noise (S/N) of their spectra and the possibility of getting multiwavelength coverage, which can help in the data interpretation. In Mingozzi et al. (2022) (Paper IV hereafter) we have started to create such a UV toolkit using the Cosmic Origins Spectrograph (COS) Legacy Archive Spectroscopic SurveY (CLASSY;[28] Berg et al. 2022; James et al. 2022, Paper I and Paper II hereafter). CLASSY represents the first high-quality, high- resolution far-UV (FUV, 1150–2000 Å) Treasury of 45 nearby ($0.002 < z < 0.182$) star-forming galaxies, with properties that make them representative at all redshifts (see Paper I Figure 8), but generally characterized by more extreme ionization fields, lower stellar masses, and higher SFRs than $z \sim 0$ objects, as typically observed in the EoR (e.g., Wise et al. 2014; Madau & Haardt 2015; Robertson et al. 2015; Stanway et al. 2016; Stark 2016). Specifically, in Paper IV we provided detailed measurements of dust attenuation ($E(B-V)$), electron density (n_e), electron temperature (T_e), gas-phase metallicity ($12 + \log(\mathrm{O/H})$) and ionization parameter ($\log(U)$), using both UV and optical direct diagnostics, taking into account the different ionization zones of the ISM. Then, from the comparison of the derived properties, we provided a set of equations to estimate ISM properties only from UV emission lines. This paper presents the second part of the UV-based toolkit introduced in Paper IV and aims at exploring the well-known optical emission-line diagnostics tracing the different ionization sources and the recently proposed UV-based counterparts, to check their consistency and reliability to discriminate SF from AGN and shock ionization.

In Section 2 we describe the CLASSY sample, summarizing the characteristics of the UV and optical data, the main steps of the data analysis performed in Paper IV, while in Section 3, we give an overview of the models used in this work to interpret the optical and UV diagnostics. In Section 4 we present the main optical-diagnostic diagrams sensitive to the ionization source to demonstrate that CLASSY galaxies are indeed dominated by SF. CLASSY represents the local reference sample of metal-poor star-forming galaxies that we can use to explore the boundaries of the SF locus in UV diagnostic diagrams, as we show in Section 5, interpreting the results taking into account ISM properties and state-of-the-art photoionization and shock models. Then, in Section 6 we discuss the conditions needed to observe UV emission lines, possible caveats in using them as diagnostics and which of them are currently observed with JWST at high-z. Finally, in Section 7 we summarize our main findings. Throughout this work we assume a flat λCDM cosmology ($H_0 = 70$ km^{-1} s^{-1} Mpc, $\Omega = 0.3$) and $12 + \log(\mathrm{O/H})_\odot = 8.69$ (Asplund et al. 2009).

[28] https://archive.stsci.edu/hlsp/classy

2. The CLASSY Survey

The 45 local galaxies from the CLASSY survey span a wide range of stellar masses ($6.2 < \log(M_\star/M_\odot) < 10.1$), SFRs ($-2 < \log(\mathrm{SFR}/M_\odot\ \mathrm{yr}^{-1}) < +1.6$), oxygen abundances ($7 < 12 + \log(\mathrm{O/H}) < 8.8$), electron densities ($10 < n_e([\mathrm{S\,II}]\ \lambda\lambda6717,31)/\mathrm{cm}^{-3} < 1120$), degree of ionization ($0.54 < \mathrm{O3O2} < 38.0$, with $\mathrm{O3O2} = [\mathrm{O\,III}]\ \lambda\lambda5007/[\mathrm{O\,II}]\ \lambda\lambda3727,9$), and reddening values ($0.02 < E(B-V) < 0.67$). In Paper I, we present our sample, explaining in detail the selection criteria along with an extensive overview of the HST/COS and archival optical spectra. In addition, Paper I broadly compares the global properties of the CLASSY galaxies with local and high-z samples (see Paper I Section 5, Figure 8), showing that these objects are characterized by similar low masses and metallicities to the dwarf galaxies of the local volume, but are characterized by higher SFRs and sSFRs, consistent with high-z systems. CLASSY objects also follow the same trend as other $z \sim 0$ star-forming galaxies in the mass–metallicity relation but with a larger scatter. Recent JWST studies have further confirmed that such characteristics are typical of the high-z Universe (see e.g., Figures 4 and 5 of Curti et al. 2023; Atek et al. 2023; Simmonds et al. 2024). The data reduction is presented in Paper II, including spectra extraction, coaddition, wavelength calibration, and vignetting. In Paper IV, we explained in detail the data analysis, from the stellar continuum modeling to the emission-line fitting, providing measurements for the UV redshifts (z_{UV}), the main UV and optical emission-line fluxes and equivalent widths, and ISM properties. In the following subsections, we summarize the most important characteristics of the sample and the main steps of the data analysis performed in these previous works.

2.1. The Sample

CLASSY spectra span from 1150 to 2100–2500 Å, combining the G130M, G160M, G185M, G225M, and G140L HST/COS gratings, from 135 orbits of new COS data (PID: 15840, PI: Berg) and 177 orbits of archival COS data, for a total of 312 orbits. Both this paper and Paper IV focus on the analysis of all the emission lines (except for Lyα) in the range 1150–2000 Å, using the so-called high resolution (HR: G130M+G160M; $R \sim 10{,}000$–$24{,}000$) and moderate resolution (MR: G130M +G160M+G185M/G225M; $R \sim 10{,}000$–$20{,}000$) coadded spectra,[29] presented in detail in Berg et al. (2022).[30] We also collected data for the entire CLASSY sample in the optical wavelength regime, gathering SDSS spectra if available, integral-field spectroscopy data (VLT/VIMOS, MUSE, Keck/KCWI), or long-slit spectra (MMT; LBT/MODS, see Arellano-Córdova et al. (2022b), CLASSY Paper V). A full description of the CLASSY optical dataset can be found in Paper IV.[31]

In Paper IV and throughout this work, we take into account the properties of the CLASSY galaxies in terms of redshift, stellar mass $M_\star$, SFR, and $12 + \log(\mathrm{O/H})$, estimated and described in Paper I (see Section 4.5 and 4.7). Specifically, $12 + \log(\mathrm{O/H})$ measurements are based on the direct T_e method, using [S II] $\lambda6717/\lambda6731$ and [O III] $\lambda4363/\lambda5007$ as electron density and temperature tracers, respectively. We

[29] The instrumental broadening at the wavelengths of the emission lines taken into account in the HR and MR spectra is, respectively, $\sigma_{\mathrm{int}} \sim 15$–$30$ km s^{-1}.
[30] We only used the so-called low resolution (LR: G130M+G160M+G140L or G130M+G160M+G140L; $R \sim 1500$–4000, $\sigma_{\mathrm{int}} \sim 80$ km s^{-1}) coadds for J1044+0353 and J1418+2102 because of the lack of higher resolution data.
[31] The instrumental broadening of the optical data is in the range $\sigma_{\mathrm{int}} \sim 35$–$120$ km s^{-1}.

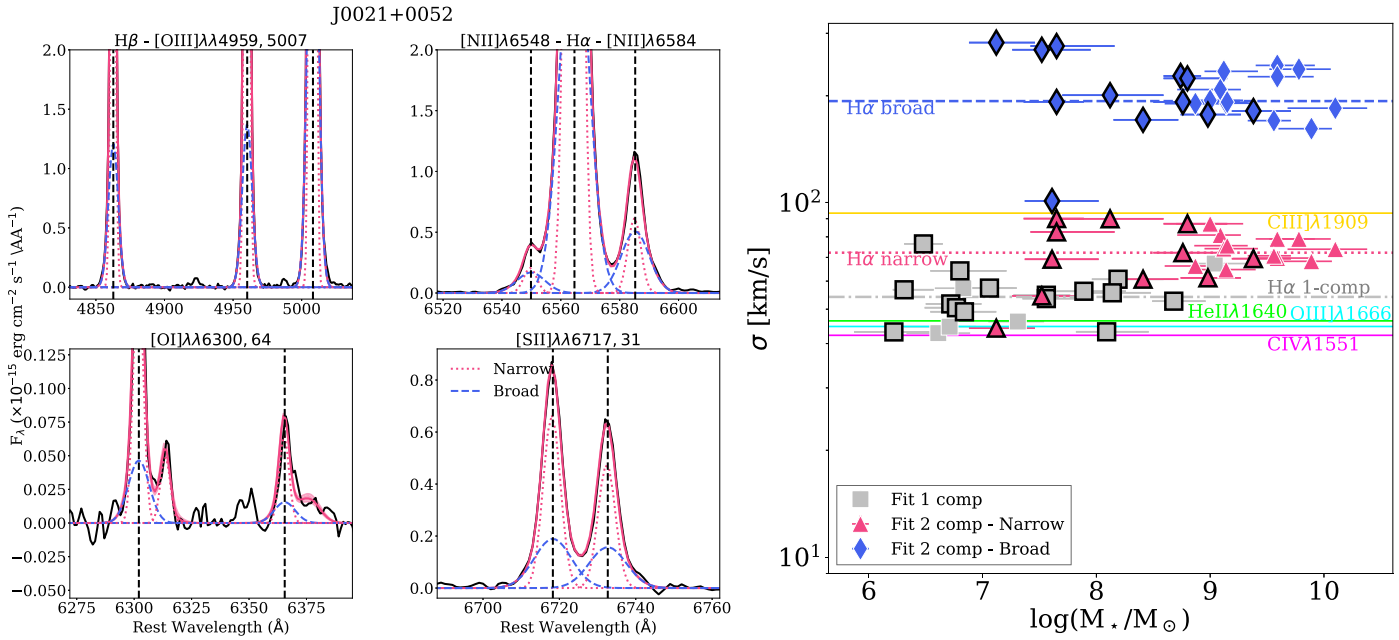

Figure 1. Left-hand panel: optical emission lines best fit with narrow and broad Gaussian components (dotted-red and dashed-blue lines, respectively; the total fit is shown by the solid-red line) for one of the CLASSY galaxies, J0021+0052. Here we show the lines needed to create the classical optical BPT diagrams (Hβ, [O III] $\lambda\lambda$4959,5007, [N II] $\lambda\lambda$6548,84, Hα, [O I] $\lambda\lambda$6300,64, [S II] $\lambda\lambda$6717,31) to discriminate among different ionization sources (see Section 4). The emission line next to [O I] λ6300 is [S III] λ6312, while the one next to [O I] λ6364 is Si II λ6371. Right-hand panel: intrinsic velocity dispersion σ (y-axis in log scale) for the one-component (gray squares) and, when needed, the two-component best fit (narrow and broad components shown as red triangles and blue diamonds, respectively) of optical emission lines, as a function of the stellar mass. The broad component σ (median value $\sim$190 km s^{-1}, dashed-blue line) is generally larger than the narrow ($\sim$70 km s^{-1}, dotted-pink line) and single ($\sim$55 km s^{-1}, dashed–dotted-gray line) components. Galaxies with at least one S/N >3 UV emission line (i.e., C III] $\lambda\lambda$1907,9; 12 + log(O/H) $\lesssim$8.3) are highlighted by a thick black edge. The UV lines intrinsic σ median values are generally consistent with the optical, as shown by the solid horizontal lines: C IV $\lambda\lambda$1548,51 (magenta), He II λ1640 (green), O III] $\lambda\lambda$1661,6 (cyan), C III] $\lambda\lambda$1907,9 (gold).

also take into account the ionization parameter log(U) from [O III] λ5007/[O II] $\lambda\lambda$3727 and the stellar age of our targets, determined from the analysis presented in Paper IV. For this paper, we also measured the carbon-to-oxygen abundance C/O, which we calculated following the prescriptions of Berg et al. (2016). Specifically, we calculated the ionic abundances of C^{++} and O^{++} from C III] λ1907,9/Hβ and [O III] λ1666/Hβ using `PyNeb`(Luridiana et al. 2015) and T_e([O III]). We then divided one by the other multiplying per the ionization correction factor (ICF), provided by Berg et al. (2016), taking into account log(U). We find $(C/O)/(C/O)_\odot$ to vary in the range 0.1–0.6, with $(C/O)_\odot = 0.44$. A detailed discussion about CLASSY C/O will be given by D. A. Berg et al. (2024, in preparation).

2.2. Data Analysis

Here, we briefly summarize the main steps of the data analysis of UV and optical spectra performed in Paper IV (see their Section 3). In particular, we used a set of customized Python scripts to first fit and subtract the stellar component, and then fit the main emission lines with multiple Gaussian components where needed.

As a preliminary step, both UV and optical CLASSY spectra were corrected for the total Galactic foreground reddening along the line of sight of their coordinates with the Cardelli et al. (1989) reddening law (see Paper I). We then fitted and subtracted the UV and optical stellar components, adopting the latest version of the Bruzual & Charlot (2003) models (S. Charlot & G. Bruzual, in preparation, hereafter C&B), assuming the Chabrier (2003) initial mass function (IMF), as described in detail in Paper IV Section 3.1. Finally, we performed the fit of the main UV and optical emission lines separately. In particular, we simultaneously fitted each spectrum taking into account a set of UV (from [N IV] λ1483, N IV] λ1487, to [C III] λ1907, C III] λ1909) and optical emission lines (from [O II] $\lambda\lambda$3727 to [S III] λ9069) with a linear baseline centered on zero and a single Gaussian, making use of the MPFIT code (Markwardt 2009), which performs a robust nonlinear least squares curve fitting (see Paper IV Section 3.2 for more details).

We noted that the Hα line in particular shows a broad component in many CLASSY galaxies (as shown in the top panel of Figure 1 for J0021+0052). Therefore, we performed two-component Gaussian fits to the main optical emission lines, i.e., [O II] $\lambda\lambda$3727,9, Hδ, Hγ, Hβ, [O III] $\lambda\lambda$4959,5007, [O I] $\lambda\lambda$6300,74, [N II] $\lambda\lambda$6548,84, Hα, [S II] $\lambda\lambda$6717,31. In particular, we used a narrow ($\sigma < 200$ km s^{-1}) and a broad ($\sigma < 1000$ km s^{-1}) Gaussian component, tying the velocity and velocity dispersion of each component to be the same for all the emission lines. We applied a reduced chi-square selection to state if a fit with a second component better reproduces the observed spectral profiles (see Section 3.2.2 of Paper IV for more details). Overall, a second broad component is needed in 24 out of 45 galaxies of our sample. This component tends to be slightly blue-shifted ($\sim$50–80 km s^{-1}) at increasing $M_\star$ and accounts for $\lesssim$30% of the total emission (Paper IV).

The right-hand panel of Figure 1 shows the intrinsic velocity dispersion σ that we calculate from the optical emission lines as a function of the galaxy stellar mass for our sample.[32] In particular, we show either the single-Gaussian σ (gray squares)

[32] The emission-line velocity dispersion σ refers to the Hα line for the optical and is corrected for the instrumental broadening $\sigma_{\rm int}$ of the different instruments taken into account, assuming $\sigma = \sqrt{\sigma^2_{\rm obs} - \sigma^2_{\rm int}}$.

or the narrow (red triangles) and broad component (blue diamonds) σ, according to the best fit selected for each galaxy. The median values of the single, narrow, and broad components are ∼55, ∼70, and ∼190 km s^{-1}, respectively, as indicated by the dashed–dotted-gray, dotted-red, and dashed-blue horizontal lines. The single-Gaussian σ for the objects that need a two-component fit is not shown, but its median value would be ∼100 km s^{-1}, and thus much higher than the value calculated for the narrow component. Overall, the broad emission component can trace gas at different velocities along the line of sight due to different mechanisms, including stellar winds, galactic outflows or turbulence, linked to different ionization sources (e.g., stellar or AGN photoionization and/or shocks; Izotov & Thuan 2007; James et al. 2009; Amorín et al. 2012; Bosch et al. 2019; Hogarth et al. 2020; Komarova et al. 2021). Hence, in Section 4 we use σ to explore whether correlations exist between gas kinematics and the optical diagnostics tracing the level of ionization of the gas (e.g., Kewley et al. 2019).

In Figure 1, the CLASSY targets with at least one UV emission line (i.e., C III] λλ1907,9) are highlighted by a thick black edge: they all have generally low stellar masses and 12 + log(O/H) ≲8.3. C III] λλ1907,9 is the most common UV emission line in CLASSY galaxies (observed in 28 objects) without considering Lyα (see Hu et al. 2023 or Paper VII) because it is usually seen in low-mass SFGs (e.g., Rigby et al. 2015; Du et al. 2017; Maseda et al. 2017). Specifically, all the CLASSY galaxies showing either He II λ1640 (19) or O III] λ1666 (22) also have C III] emission (see Paper IV). In addition, these three emission lines are all visible in the nine CLASSY galaxies characterized by C IV λλ1548,51 in pure emission. The colored solid horizontal lines in Figure 1 indicate their median intrinsic velocity dispersions, which we calculated, taking into account COS instrumental resolution, as well as the extension of the sources derived from the COS NUV acquisition images (see Paper II Sections 2 and 3.2; James et al. 2014 Section 3.2). In general, He II λ1640, O III] λ1661, 6 and C IV λλ1548,51 share very similar values ($\sigma \sim 50$ km s^{-1}), consistent with optical emission lines at similar stellar masses. We will further comment on this in Section 6. We emphasize that the UV emission-line S/N is typically not high enough to detect faint broad components in the emission lines, apart from a few exceptions that show broad emission in C IV λλ1548,51, He II λ1640 and [O III] λλ1661,6 (but not in C III]) (Paper IV, Section 3.3.). In addition, UV lines are not seen in the most massive targets in which the optical line broad components are particularly enhanced. However, the fact that σ(C III]) is systematically higher than other UV lines (σ(C III]) ∼90 km s^{-1}) could indicate the presence of a hidden undetected broad component. A further discussion of the optical and UV kinematical properties of the sample can be found in Appendix A.

3. Diagnostic Models Used within This Work

This work aims to understand how state-of-the-art models from the literature compare to observed line ratios of the CLASSY survey, using well-studied optical diagnostics and less well-constrained UV diagnostics. This section provides an overview of each model considered for the main sources of ionization found within galaxies: photoionization, AGN, and shocks. We provide a summary of the models taken into account in Table 1. In the next sections of the paper, we investigate and comment on optical and UV diagnostics to distinguish between these different ionizing mechanisms.

Concerning stellar photoionization grid models (referred to as SF models hereafter), we take into account emission from H II regions around young stars, using nebular-emission models of SFGs from Gutkin et al. (2016) (G16 hereafter) based on two limiting cases: one instantaneous burst (single stellar population; SSP models) or constant activity with time (CST models). In particular, single-burst models, in which the emission is strongest at young ages (i.e., from 3–4 Myr up to 5–7 Myr if stellar rotation is included) and disappears as the massive star population evolves, are generally used for young stellar populations and very recent starbursts, and are thus more consistent with the CLASSY galaxies and EoR systems. G16 models do not take into account either stellar rotation or stellar multiplicity, which would imply a longer duration of ionizing photon production (e.g., MIST models from Byler et al. 2017 models) and in the latter case a harder radiation field, e.g., binary population and spectral synthesis (BPASS) models from Xiao et al. (2018). Other possible differences between G16 and other models in the literature concern the choice of stellar libraries, IMF, or the way to scale gas-phase metallicity for elements such as nitrogen and carbon.[33] For the purpose of this study, we take into account G16 models (with constant and burst of SF), BPASS models from Xiao et al. (2018) [34] (X18 hereafter), and Byler et al.'s (2017) (B17 hereafter) models. G16 model parameters (see Table 1) are well matched with the AGN and shock grids that we present below, allowing us to make a consistent comparison between optical and UV diagnostic diagrams. Meanwhile, X18 and B17 models allow us to explore the differences caused by the inclusion of interacting binary stars in the stellar population and stellar rotation, respectively (and thus a harder radiation field), as we show in Section 5 and Appendix C.1.

As shown in Feltre et al.'s (2016) Figure 1, the ionizing spectrum powered by a lower metallicity stellar population is harder with respect to a more metal-enriched stellar population, producing a different spectral energy distribution at photon energies greater than ∼20 eV. However, it generally cannot account for ionic species with ionization energies above ∼50 eV. Hence, the presence of emission lines requiring such ionization energy could be a good indicator of the presence of an additional ionization mechanism than SF (e.g., AGN or shocks). In this work, we take into account the AGN models from Feltre et al. (2016) (F16 hereafter).

The main parameters in F16 models are the slope α of the ionizing spectrum,[35] as well as the other quantities shown in detail in Table 1. Collisional excitation and photoionization from slow ($v \lesssim 150$ km s^{-1}) and fast shocks ($v \sim 150$–1000 km s^{-1}), respectively, can also produce a rich spectrum of UV and optical emission lines because shocked regions have high electron temperatures and ionization states (Dopita & Sutherland 2003). Here we take into account the shock models from the 3MdBs[36] database (Alarie & Morisset 2019; AM19). These model grids span a broad range of metallicities, matched with G16 grid

[33] The former has secondary nucleosynthetic production at high metallicity, while part of the latter returns to the ISM through metallicity-dependent processes such as stellar winds (see e.g., Byler et al. 2018 for more details).
[34] http://www.bpass.auckland.ac.nz
[35] The luminosity per unit frequency S_ν of the AGN accretion disk is usually approximated by a broken power law, with $S_\nu \sim \nu^\alpha$ at wavelengths $0.001 \leqslant \lambda/\mu \leqslant 0.25$, as shown in Equation (5) of F16.
[36] http://3mdb.astro.unam.mx/

Table 1
Summary of the Models Used in This Work

Model	Parameters	Sampled Values	Notes
G16	Ionizing spectrum	CST SF; age =100 Myr	Bruzual & Charlot (2003) stellar pop. synthesis models + Cloudy (Ferland et al. 2013). The values of gas-phase metallicity correspond to 12 + log(O/H) =6.64, 7.64, 8.55, 8.88 and log($Z_{ISM}/[Z_\odot]$) −2.2−0.04. We tested all values of n_H, ξ_d, and (C/O), but here we show only $n_H = 100$ cm^{-3}, $\xi_d = 0.3$, and (C/O)/[(C/O)$_\odot$] =0.1, 0.72. Special prescriptions for C and N because scale nonlinearly with O (G16 Section 2.3.1; see Henry et al. 2000; Berg et al. 2016).
	Z_{ISM}	0.0001,0.001,0.008,0.017; $Z_\odot = 0.01524$	
	log(n_H/[cm^{-3}])	1, 2, 3, 4	
	log(U_S)	−3.5, −3., −2.5, −2., −1.5, −1.	
	ξ_d	0.1, 0.3, 0.5	
	(C/O)/[(C/O)$_\odot$]	0.10, 0.14, 0.20, 0.27, 0.38, 0.52, 0.72, 1.00, 1.40; (C/O)$_\odot = 0.44$	
	IMF	Chabrier (2003) (0.1 $M_\odot$; m_{up} = 100.,300. $M_\odot$)	
G16	Ionizing spectrum	SSP; age = 1–10 Myr	Same as in CST G16 grids. Given the absence of stellar rotation and multiplicity, the ionizing radiation drops at older ages than 5 Myr. All the parameters are as in CST models. In this work, we show only grids with t = 3, 5, 10 Myr.
X18	Ionizing spectrum	SSP; age = 1–100 Myr	BPASS V2.1 population models (Stanway et al. 2016; Eldridge et al. 2017) + Cloudy (Ferland et al. 2013). The gas nebula is assumed without dust and a constant n_H with 12 + log(O/H) =6.6, 7.61, 8.52, 8.93 (matched to $Z_\star$). In this work, we show only grids with $n_H = 100$ cm^{-3} and t = 3, 10 Myr. C, N, and other elements fractions are scaled according to the population metallicity Z (see Table 2, Xiao et al. 2018).
	Z_{ISM}	0.0001, 0.001, 0.008, 0.020; $Z_\odot = 0.020$	
	log(n_H/[cm^{-3}])	0–3 in 0.5 dex intervals	
	log(U_S)	−3.5, −3. , −2.5, −2. , −1.5	
B17	Ionizing spectrum	Bursts of SF; age t = 0.5, 1, 2, 3, 4, 5, 6, 7, 10 Myr	MESA Isochrones & Stellar Tracks + Cloudy + Flexible Stellar Population Synthesis code (Byler 2018). Stellar rotation and nebular line and continuum emission included. Ionizing radiation is strong at young ages (up to 5–7 Myr) and disappears as massive stars evolve. Larger metallicity range than G16 (12 + log(O/H) ∼6.93–8.68). In this work, we show only t = 3, 5, 10 Myr.
	log($Z_{ISM}/[Z_\odot]$)	−1.5, −1.0, −0.6, −0.4, −0.3, −0.2,0.1, 0.0, 0.1, 0.2; $Z_\odot = 0.0142$	
	n_H/[cm^{-3}]	100.	
	log(U_S)	Same as G16	
	IMF	Kroupa (2001) ($m_{min} = 0.1$ $M_\odot$; $m_{up} = 120.$ $M_\odot$)	
	Others	N and C treated with equations reported in Byler et al. (2017).	
F16	Ionizing spectrum	AGN NLR; α = 1.2, −1.4, −1.7, −2.0	Cloudy models with open geometry, luminosity $L_{AGN} = 10^{45}$ erg s^{-1}, inner radius from the NLR of 300 pc. Ionizing spectrum parameterized with the power-law index α of the spectral energy distribution of the incident ionizing radiation from the AGN accretion disk at UV and optical wavelengths in AGN models. All heavy elements except for nitrogen (see F16 Equation 6) are assumed to scale linearly with oxygen abundance.
	Z_{ISM}	Same as G16	
	n_H/[cm^{-3}]	Same as G16	
	log(U_S)	Same as G16	
	ξ_d	Same as G16	
AM19	Ionizing spectrum	Fast shocks ($v_s > 100$ km s^{-1})	Mappings-V (Sutherland & Dopita 2017) and a plane-parallel geometry. Models created using same prescriptions of the well-known Allen et al. (2008) shock models by AM19, but using the metallicity values of G16, to study variation with metallicity. We tested all values, but in this paper we show only grids with $n_H = 1$ cm^{-3}, (C/O)/(C/O)$_\odot = 0.26$ for $Z_{ISM} = 0.0001$, 0.001 and (C/O)/(C/O)$_\odot = 1.00$ for $Z_{ISM} = 0.017$ (trans-solar metallicity grid).
	Z_{ISM}	0.0001, 0.001, 0.008, 0.08, 0.017	
	n_H/[cm^{-3}]	1., 10., 100., 1000., 10000.	
	v_s/[km s^{-1}]	100, 125, ⋯, 1000	
	(C/O)/[(C/O)$_\odot$]	0.26, 1.00	
	$B_0/[\mu$G]	10^{-4}, 0.5, 1.0, 2.0, 3.23, 4.0, 5.0, 10	

Note. Constant (CST) and single-burst (single stellar population; SSP) Gutkin et al. (2016) grids (G16) and Xiao et al. (2018) BPASS models (X18) for SF, Feltre et al. (2016; F16) for AGN narrow-line region (NLR), Alarie & Morisset (2019; AM19) for shocks. The parameters include the ionizing spectrum, gas-phase metallicity (Z_{ISM}), ionization parameter log(U_S), dust-to-gas ratio (ξ_d), carbon-to-oxygen abundance (C/O), and initial mass function (IMF). ξ_d accounts for the depletion of metals onto dust grains in the ionized gas. We refer to Section 4 of Plat et al. (2019) to see the impact of the variation of the parameters that we fix in this work.

values (see Table 1), with respect to the well-known MAPPINGS models from Allen et al. (2008),[37] and thus are the best suited for the CLASSY sample. The emission-line spectra primarily depend on the shock velocity v_s and the magnetic field parameter B_0, which regulate the shock ionization spectrum and the effective ionization parameter. An increase in the density of the material preceding the shock ionization front (preshock density n_H) can also play a role because it enforces the collisional de-excitation of forbidden lines. Generally, two sets of models are taken into account: shocks and shocks+precursor. The precursor emission becomes important at increasing velocities of the shock front ($v \gtrsim 170$ km s^{-1}), where the ionization front velocity exceeds v_s. Indeed, the high velocity causes the photoionization front to detach from the shock and form a "precursor," which can contribute to or even dominate the shock emission. In general, we noticed that an increase in density from $n_H \sim 1$ cm^{-3} to $n_H \sim 1000$ cm^{-3} does not lead to dramatic changes in the optical and UV line ratios, as discussed in the following sections unless noted in the text. Hence, in this work, we only show grids with $n_H = 1$ cm^{-3} (consistently with shock grids usually shown in other works; e.g., Allen et al. 2008). In addition, at subsolar metallicities, we show the grids with $(C/O)/(C/O)_\odot = 0.26$, which are also more consistent with the properties of the CLASSY galaxies.

4. Results: Optical Diagnostics Sensitive to the Ionization Source

In this section, we present the most frequently used classification methods in the optical, showing and discussing where the CLASSY galaxies are located in different diagnostic diagrams. In particular, we compared different criteria to discriminate between ionization processes, sometimes finding that there is no one-to-one agreement in classification, especially for low-mass and low-metallicity galaxies (e.g., Groves et al. 2006; Shirazi & Brinchmann 2012; Sartori et al. 2015; Nakajima & Maiolino 2022; Polimera et al. 2022). In Table 2, we summarize the explored optical diagnostics and the corresponding classifications for each galaxy. Overall, a combination of criteria represents the best way to provide a robust determination of the main ionization source.

Before going into the details listed in this section, here we disclose our main results about optical diagnostics. In this work, we find that CLASSY galaxies are characterized by [O III]/Hβ narrow and broad components typical of star-forming galaxies. Furthermore, their broad components—if present—have enhanced [N II]/Hα (and slightly enhanced [S II]/Hα and [O I]/Hα) and [O I]/[O III] (possible shock evidence) but lower [O III]/[O II] (i.e., lower level of ionization) and do not show a trend with He II λ4686 (that could be enhanced by shocks/AGN). We do not preclude that a few of them can have shocks (and possibly hidden AGN activity in the trans-solar galaxy J0808+3948) but, in general, the main ionizing mechanism is clearly SF. This conclusion is not surprising given that the sample was selected excluding targets with a classification other than star-forming, but here we further confirmed it by exploring different diagnostic diagrams.

Performing this optical-diagnostic test is important because in Section 5 we test how the UV diagnostic diagrams compare to the well-known and reliable optical ones presented here. In the following plots, we highlight the objects with at least one UV line detection with a thick black edge (i.e., S/N (C III] $\lambda\lambda$1907,9) >3) because only a subsample of low-metallicity objects show UV emission lines.

4.1. The Classical Optical BPT Diagrams

The three panels of Figure 2 illustrate the [N II], [S II] and [O I]–BPT diagrams for the single (gray squares), narrow (red triangles), and broad (blue diamonds) components of the CLASSY galaxies. The SF models are not shown for clarity reasons but can completely cover the classical SF locus, while the F16 models predict higher [O III]/Hβ, consistently with the classical AGN locus. According to these diagnostics, the majority of the CLASSY galaxies are dominated by SF, even though the classification is not always consistent among different diagnostics, with many objects at the edge of the SF locus (indicated by the solid-black maximum starburst line). In particular, at these edges we mainly find the CLASSY objects characterized by UV emission lines (highlighted by thick black edges), which have generally higher [O III]/Hβ than the others and low gas-phase metallicity ($12 + \log(O/H) \lesssim 8.3$, corresponding to $Z \lesssim 50\%\ Z_\odot$). However, as we discuss in the following paragraphs, two main factors can affect the definition of the SF locus and need to be taken into account: the metallicity and the hardness of the radiation field.

On the one hand, [N II]/Hα is particularly sensitive to metallicity (Denicoló et al. 2002; Kewley & Dopita 2002; Pettini & Pagel 2004; Kewley & Ellison 2008), with lower [N II]/Hα at decreasing metallicity (see, e.g., the CLASSY galaxies J1323-0132 and J0808+3948 in Paper V Figure 2). Since higher [N II]/Hα line ratios are required to classify galaxies as AGN, the [N II]–BPT by itself is not sufficient for identifying AGN in typical low-metallicity star-forming $z \sim 0$ galaxies (e.g., Groves et al. 2006; Reines et al. 2020; Molina et al. 2021; Polimera et al. 2022). For instance, Polimera et al. (2022) showed that the [O I]–BPT[38] can identify a theoretical dwarf AGN with a spectrum characterized by ~90% SF contribution and classified as star-forming according to the [N II]–BPT (see also Hogarth et al. 2020). Indeed, [O I]/Hα is highly sensitive to hard radiation fields, particularly shock emission in the neutral ISM (e.g., Osterbrock & Ferland 2006; Allen et al. 2008), and is not very dependent on metallicity. Hence, an [O I]/Hα enhancement could suggest that there is an additional excitation mechanism other than stellar photoionization that is missed by the [N II]–BPT diagram. Looking at Table 2, some galaxies are classified as SF-dominated according to the [N II]–BPT and as AGN according to the [O I]–BPT because they are located slightly beyond the Kewley et al. (2006) maximal starburst line. However, here we stress that the [O I] λ6300 line is fainter than [N II] and [S II], and thus the [O I]/Hα line ratio has larger error bars, as shown in Figure 2.

On the other hand, low-metallicity stellar populations produce harder radiation fields and thus higher [O III]/Hβ (and lower low-ionization line ratios) without the need to invoke other mechanisms than SF (e.g., Feltre et al. 2016; Byler et al. 2018; Xiao et al. 2018). In this context, X18 explored the variation of the maximal starburst line (i.e., the highest line ratios reproduced with SF models) in BPT diagrams as a function of the metallicity, using pure stellar

[37] AM19 models are made with MAPPINGS-V and agree with Allen et al. (2008) predictions at LMC metallicity (see AM19 for more details).

[38] Polimera et al. (2022) also tested the [S II]–BPT diagram, which resulted in being less sensitive to SF dilution compared to the [O I]–BPT.

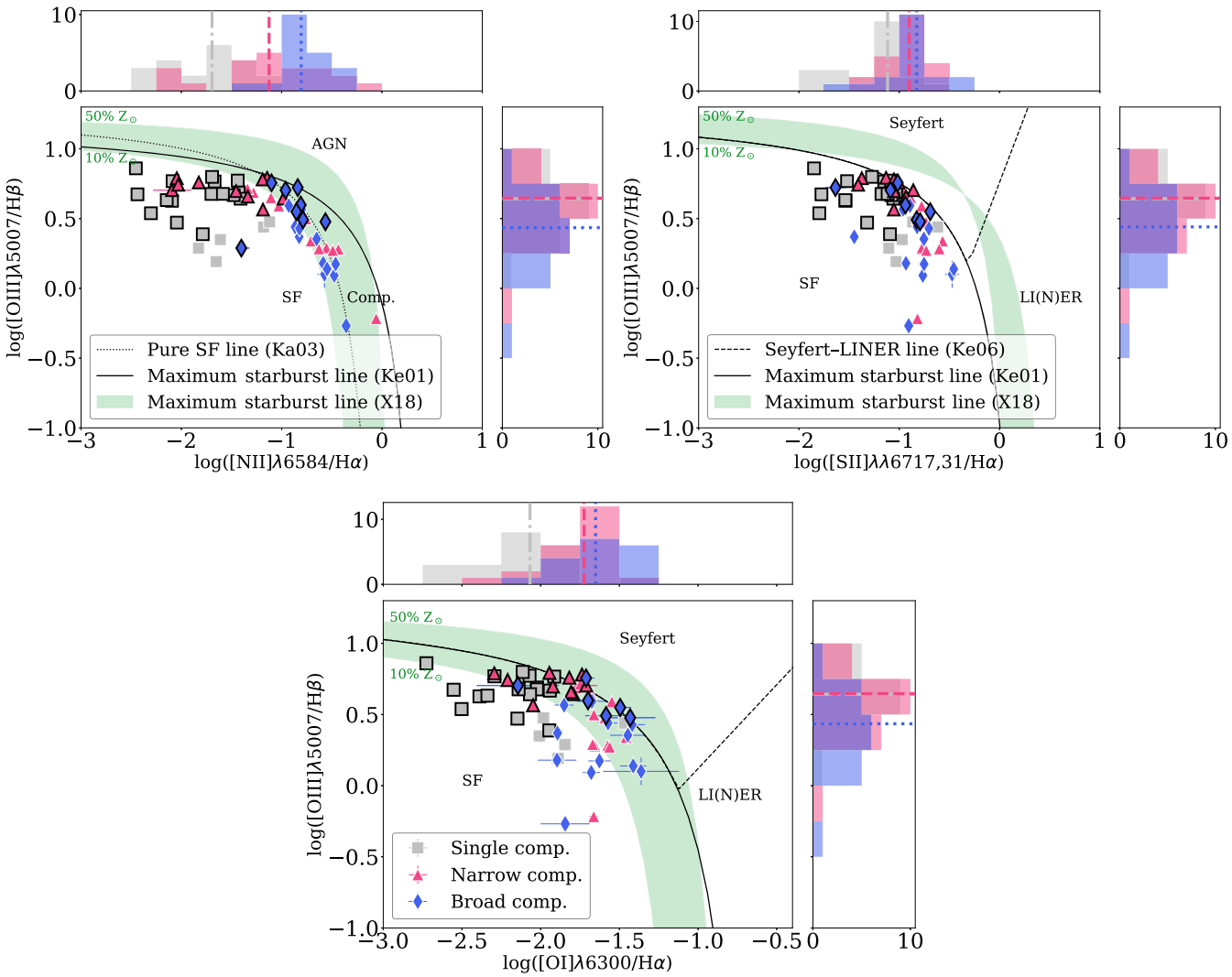

Figure 2. [N II] (top left-hand panel), [S II] (top right-hand panel), and [O I] (bottom panel) BPT diagrams for the single, narrow and broad components, shown as gray squares, red triangles, and blue diamonds, respectively. All the measurements have S/N > 3 for all the lines involved. The dotted-black curve is the empirical relation to divide pure star-forming from Seyfert-H II composite objects by Kauffmann et al. (2003), while the solid-black curves are the maximum starburst line derived by Kewley et al. (2001). The dashed-black lines are the Kewley et al. (2006) boundary between Seyferts and low-ionization (nuclear) emission-line regions (LI(N)ERs; see also Heckman 1980; Belfiore et al. 2016). Histograms showing the distribution of [N II]/Hα, [S II]/Hα, [O I]/Hα, and [O III]/Hβ line ratios in the single, narrow and broad components are shown in gray, red and blue, respectively, on each axis, with median values shown by the dashed–dotted-, dashed-, and dotted-black lines. The broad component clearly shows higher *x*-axis line ratios. The green-shaded regions represent the maximal starburst predictions at metallicity between 10% $Z_{\odot}$ and 50% $Z_{\odot}$ values, using pure stellar photoionization including massive star binaries through the BPASS stellar evolution models (Xiao et al. 2018), to show the extent to which the maximal starburst line can change in the metallicity range in which we observe UV emission lines. According to the updated BPT separators from X18, thus taking into account the gas-phase metallicity of each target, all the galaxies are classified as SF dominated. The galaxies with at least one UV emission line (i.e., C III] λλ1907,9) are highlighted by a thick black edge.

photoionisation including massive star binaries through the BPASS (Eldridge & Stanway 2009) stellar evolution models.[39] The green-shaded regions in Figure 2 show the predictions of the X18 maximal starburst lines between $Z \sim 10\% Z_{\odot}$ and $Z \sim 50\% Z_{\odot}$ to underline how difficult the separation between different ionization mechanisms can be for galaxies that lie very close to the edges of the classical BPT diagrams in this range of metallicity (at which we observe also the UV emission lines we discuss in Section 5). Overall, we stress that taking into account the criteria of X18 and the gas-phase metallicity measured for each object of our sample, all the galaxies are classified as SF dominated.

Another interesting implication from Figure 2 is that the broad component of our galaxies is usually characterized by higher [N II]/Hα and [O I]/Hα, slightly higher [S II]/Hα, and slightly lower [O III]/Hβ line ratios. This difference is shown by the gray, red, and blue histograms on each axis of Figure 2, and is more enhanced when comparing results of the single-Gaussian fit with the broad component of the two-Gaussian fit (up to ∼1 dex in log([N II]/Hα) and ∼0.5 dex in log([O I]/Hα)). In particular, strong low-ionization lines could be a signature of shocks (Osterbrock & Ferland 2006). In addition, the broad component has (by definition) a much larger velocity dispersion than the narrow one, as shown in Figure 1. This σ enhancement at increasing [N II]/Hα, [S II]/Hα, and [O I]/Hα

[39] Binary-star evolution pathways produce harder radiation up to older ages than single stars mainly because of the gas accretion onto compact objects (e.g., HMXBs).

Table 2
CLASSY Sample Classification

Object	Alternative Name	[N II]–BPT N/B	[S II]–BPT N/B	[O I]–BPT N/B	[O I]–[O II]–[O III] N/B	He II N/B
(1)	(2)	(3)	(4)	(5)	(6)	(7)
J0021+0052		SF/SF	SF/SF	SF/SF	SF/SF	SF
J0036-3333	Haro 11 knot C	SF/SF	SF/SF	SF/SF	SF/SF	SF
J0127-0619	Mrk 996	SF/SF	SF/NC	SF/NC	SF/NC	NC
J0144+0453	UM 133	SF/NC	AGN/NC	AGN/NC	SF/NC	SF
J0337-0502	SBS 0335-052 E	SF/NC	SF/NC	SF/NC	SF/NC	SF/NC
J0405-3648		SF	SF	SF	SF	SF
J0808+3948		Comp/SF	SF/SF	SF/SF	AGN-shocks/NC	AGN
J0823+2806	LARS9	SF/Comp	SF/SF	SF/SF	SF/SF	SF
J0926+4427	LARS14	SF/Comp	AGN/SF	AGN/SF	SF/SF	NC
J0934+5514	Izw 18	…	…	…	…	SF
J0938+5428		SF/SF	SF/SF	SF/SF	SF/SF	SF
J0940+2935		SF	SF	SF	SF	NC
J0942+3547	CG-274, SB 110	SF	SF	SF	SF	SF
J0944+3442		SF	SF	SF	AGN-SF	NC
J0944-0038	CGCG007-025	SF	SF	SF	SF	SF
J1016+3754	1427-52996-221	SF	SF	SF	SF	SF
J1024+0524	SB 36	SF	SF	SF	SF	SF
J1025+3622		SF/SF	SF/SF	AGN/SF	SF/SF	SF
J1044+0353		SF	SF	SF	SF	SF
J1105+4444	1363-53053-510	SF/SF	SF/SF	SF/AGN	SF	SF
J1112+5503		Comp/SF	SF/SF	SF/SF	SF/SF	Comp
J1119+5130		SF	SF	SF	SF	SF
J1129+2034	SB 179	SF	SF	SF	SF	SF
J1132+1411	SB 125	SF	SF	SF	SF	SF
J1132+5722	SBSG1129+576	SF	SF	SF	SF	SF
J1144+4012		SF/SF	SF/SF	SF/SF	SF	NC
J1148+2546	SB 182	SF	SF	SF	SF	SF
J1150+1501	SB 126, Mrk 0750	SF	SF	SF	SF	SF
J1157+3220	1991-53446-584	SF	SF	SF	SF	SF
J1200+1343		Comp/Comp	SF/SF	AGN/NC	SF/NC	SF
J1225+6109	0955-52409-608	SF/NC	SF/NC	SF/NC	SF/NC	SF
J1253-0312	SHOC391	…	…	…	SF/SF	NC
J1314+3452	SB 153	SF	SF	SF	SF	SF
J1323-0132		SF	SF	SF	SF	SF
J1359+5726	Ly 52, Mrk 1486	SF/SF	SF/SF	SF/SF	SF/SF	SF
J1416+1223		Comp/SF	SF/SF	SF/SF	SF/SF	NC
J1418+2102		SF	SF	SF	SF	SF
J1428+1653		SF/SF	SF/SF	SF/SF	SF/SF	NC
J1429+0643		SF/SF	AGN/SF	AGN/AGN	SF/SF	SF
J1444+4237	HS1442+4250	SF	SF	SF	SF	NC
J1448-0110	SB 61	SF	SF	SF	SF	SF
J1521+0759		SF/SF	SF/SF	AGN/SF	SF/SF	NC
J1525+0757		SF/SF	SF/SF	SF/SF	SF/SF	NC
J1545+0858	1725-54266-068	SF/Comp	SF/SF	SF/AGN	SF/SF	SF
J1612+0817		Comp/Comp	SF/SF	SF/SF	SF/SF	SF

Note. Classification according to the optical-diagnostic diagrams taken into account: [N II]–BPT (3), [S II]–BPT (4), [O I]–BPT (5), the [O I]–[O II]–[O III] discussed in Section 4.2 (column (6)), and the He II-diagram discussed in Section 4.3 (column (7)). The dominant ionization mechanism is classified as SF, composite (Comp), AGN, or, if one or more of the involved lines have S/N < 3, not classified (NC). The "…" indicates that some of the involved emission lines are out of the observed wavelength range. Columns (3), (4), and (5) report the classification using the standard separators shown in black in Figure 2. According to the updated BPT separators from X18 (shaded green in Figure 2) all of the galaxies are classified as SF dominated. None of the CLASSY galaxies are classified as a low-ionization (nuclear) region or LI(N)ER. For the optical diagnostics, we specify the classification of both the narrow (N) and (B) components, if present. The 28 galaxies in bold are those which show a 3σ detection in C III] $\lambda\lambda$1907,9 ($12 + \log(O/H) \lesssim 8.3$, $Z \lesssim 50\%\ Z_{\odot}$)

line ratios suggests that the kinematics and ionization state could be coupled, implying the same physical origin, which could be different from the one producing the narrow components. This correlation has already been found in normal star-forming galaxies and AGN (e.g., Ho et al. 2014; Mingozzi et al. 2019; Hogarth et al. 2020), and it was attributed to a shocked gas component because stellar/AGN photoionization is not expected to cause such a trend (see e.g. Dopita & Sutherland 1995; Rich et al. 2010; McElroy et al. 2015; Kewley et al. 2019. We note that the σ enhancement is more evident in [N II]/Hα, and so could also be related to a nitrogen enhancement of the more perturbed gas (e.g., James et al.

2009). We will explore this further in K. Z. Arellano-Córdova et al. (2024, in preparation).

Finally, in Appendix B we also comment on an alternative optical BPT diagnostic diagram that exploits only line ratios in the blue part of the optical spectrum (i.e., [O II] $\lambda\lambda$3727/Hβ versus [O III] λ5007/Hβ, Figure 12; Lamareille et al. 2004; Lamareille 2010).[40]

To summarize, since [O III]/Hβ is in the SF locus in the BPT diagrams (Figure 2) and is not enhanced in the broad component, we think that it is unlikely that AGN are present in our sample. Here we acknowledge that Hatano et al. (2023) recently claimed that SBS 0335-052 E hosts an AGN on the basis of a recent NIR variability and the broad Hα component. We also reveal a broad Hα component ($\sigma \sim 1000$ km s^{-1}) that is not visible in the other emission lines (this could be due to low S/N and low metallicity), but the narrow component line ratios analyzed in this work are all classified as SF-dominated. Finally, the [O I]-excess that we observe in some galaxies of the sample, as well as the increase of [N II]/Hα, [S II]/Hα, and [O I]/Hα line ratios with velocity dispersion, indicate the possible presence of additional mechanisms, such as shocks, which we further discuss in the following section.

4.2. [OI] λ6300 as a Shock Indicator

Figure 3 shows the [O III] λ5007/[O II] $\lambda\lambda$3727 versus [O I] λ6300/[O III] λ5007 diagram ([O I]–[O II]–[O III] diagram) for the CLASSY galaxies (single, narrow, and broad components shown as in Figure 2), presented as a diagnostic plot for the first time in Heckman (1980) to separate Seyferts from LINERs (see also Stasińska et al. 2015). This diagram is not very dependent on gas-phase metallicity (Stasińska et al. 2015), avoiding the drawbacks discussed for the classical [N II]–BPT diagram. Clearly, Figure 3 represents a good tool to discriminate between SF, AGN, and shocks for our sample, as also shown by the good separation of the SF, AGN, and shock model grids, with just a slight overlap between the grids at the highest [O I]/[O III] line ratios.[41] We highlight that increasing the preshock density n_H from $n_H \sim 1$ cm^{-3} to $n_H \sim 1000$ cm^{-3} would lead to higher log ([O III]/[O II]), which can increase up to $\sim$0.5–1.5 for shock +precursor and pure-shock grids, respectively. Still, shock models are generally characterized by higher log([O I]/[O III]) than AGN models, reaching values up to $\sim$1. The dashed-blue line

$$y = -0.84\,x - 1.0 \quad (1)$$

qualitatively separates the SF from AGN/shock models, while the dashed–dotted-black line indicates the AGN locus:

$$\begin{aligned} &y = -0.15 \quad \text{and} \quad -0.96 < x < -0.3 \\ &y = -1.75\,x - 0.70 \quad \text{and} \quad -3.5 < x < -0.3 \end{aligned} \quad (2)$$

with $y = \log([\text{O III}]\,\lambda5007/[\text{O II}]\,\lambda\lambda3727)$ and $x = \log([\text{O I}]\,\lambda6300/[\text{O III}]\,\lambda5007)$.

Overall, Figure 3 shows that the vast majority of the CLASSY galaxies can be reproduced by SF models, further confirming the classification obtained with the classical BPT diagrams (Figure 2). In particular, the optical line broad velocity components show a significant enhancement in terms of the [O I]/[O III] line ratio (with the broad showing a larger median value by $\sim$0.5 and $\sim$1 dex than the narrow and single components, respectively; except for J0926+4427, J1148+2546 and J1253-0312) and a lower [O III]/[O II] (in all galaxies except for J1148+2546). Shocks can naturally explain high [O I]/[O III] line ratio with high [O III]/[O II], while photoionization models that produce high [O I]/[O III] show, in turn, low [O III]/[O II] (e.g., Stasińska et al. 2015; Plat et al. 2019). This suggests that the more turbulent ionized gas also has a stellar source of ionization. The narrow components of only two CLASSY galaxies are at the edge of the SF locus defined by our Equation (1) in this diagram: J0944+3442 and J0808+3948, which could be both consistent with AGN and shock models. J0944+3442 is classified as star-forming according to the optical BPT diagrams, while only the narrow component of J0808+3948 is classified as composite according to the [N II]–BPT diagram. J0808+3948 has also an extremely high nitrogen enhancement and high N/O (K. Z. Arellano-Córdova et al. 2024, in preparation; see also Stephenson et al. 2023). We stress that these galaxies have no detections of UV lines, so are not shown in the UV diagnostic diagrams discussed in Section 5 (J0808+3948 is the only trans-solar metallicity galaxy of the sample (12 + log(O/H) $\sim$8.77); J0944+3442 has instead low metallicity (12 + log(O/H) 7.83).

Even though the [O III]/[O II] versus [O I]/[O III] diagram can be a very good tool to understand the role of shocks and separate SF from harder mechanisms, it can also have drawbacks. [O I] λ6300 is produced in the warm transition region between the fully ionized gas and neutral gas (Osterbrock & Ferland 2006; Draine 2011). As such, it traces the external parts of H II regions, close to the ionization front, where shocks and non-equilibrium heating are important (Dopita & Sutherland 2003; Dopita et al. 2013), which makes it difficult to predict [O I] λ6300 in photoionization models (Dopita et al. 2013). Furthermore, [O I] λ6300 is generally a faint emission line (this makes it even more tricky to disentangle a broad second component). Nevertheless, an observed [O I] λ6300 enhancement could still represent a sign of ionizing mechanisms other than SF. Overall, the values of the discussed oxygen line ratios are mostly consistent with SF models, further confirming the lack of strong ionizing shocks and/or AGN activity in the CLASSY galaxies.

4.3. The Shirazi–Brinchmann Diagram

To further confirm the SF classification of CLASSY galaxies, we also consider high-ionization lines such as He II λ4686. Indeed, as introduced in Section 1, Shirazi & Brinchmann (2012) proposed to use He II λ4686/Hβ versus [N II]/Hα to better constrain the ionization source. The two major advantages of this diagram (He II diagram) are that: (i) it is more sensitive to the hardness of the ionizing source than [O III]/Hβ, thus allowing a cleaner separation between star-forming and composite galaxies; and (ii) it is not particularly sensitive to the metallicity (Shirazi & Brinchmann 2012). The He II diagram for the CLASSY sample is shown in Figure 4 and is color coded as a function of 12 + log(O/H) (the broad component fit of He II λ4686 line is not detected because of the low S/N). Similarly to the standard BPT diagrams described in Section 4.1, SFGs are expected to lie below the maximum starburst (black solid) line, while AGN are located above.

[40] This diagram is useful to check two galaxies of our sample, the famous blue compact dwarf I Zw 18 (J0934+5514) and J1253-0312, which are not shown in Figure 2 because we do not have Hα coverage (see Paper IV Section 3). These two objects are classified as star-forming in Figure 12.

[41] Kewley et al. (2019) present different shock diagnostics (see their Figure 11), including one comparing [O III]/[O II] versus [O I]/Hα that we tested but excluded because the AGN and SF grids of models could not be separated as well as in Figure 3.

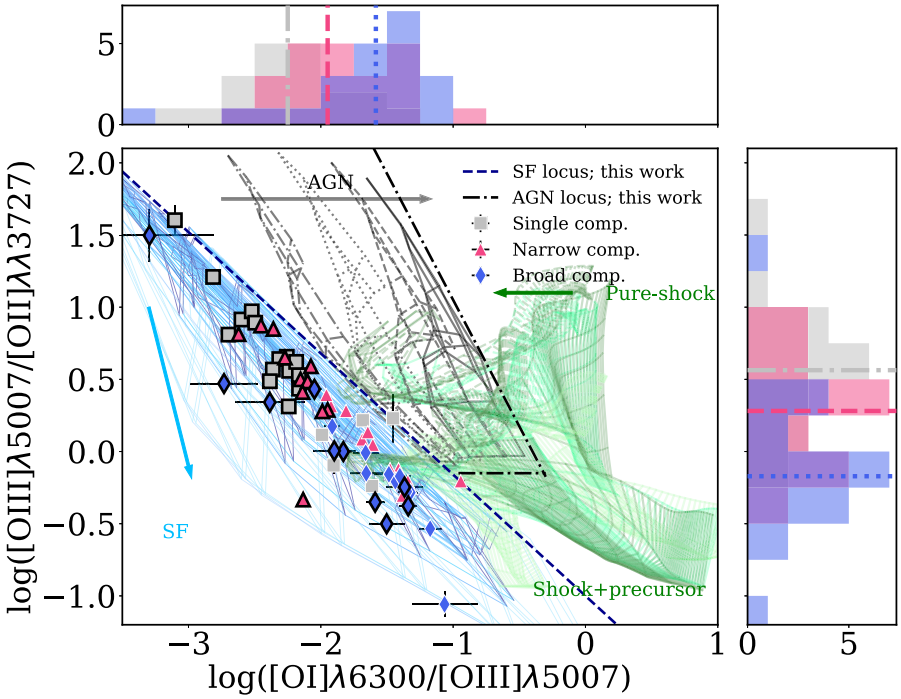

Figure 3. Location of the CLASSY galaxies in the log([O III]/[O II]) vs. log([O I]/[O III]) diagnostic diagram from Kewley et al. (2019) (see also Stasińska et al. 2015). The single, narrow, and broad components are shown as gray squares, red triangles, and blue diamonds and the histograms on the axes show their distributions and median value as in Figure 2. The blue grids show the G16 single-burst SF models, with ages of 3 Myr (darker blue) and 5 Myr (lighter blue). The G16 SF grids indicatively follow the blue arrow at increasing ages. The G16 constant SF models are not shown for clarity because they completely overlap the single-burst grids. The black grids show the F16 AGN models, with the parameter α increasing from -2 (dashed-dotted grid) to -1.2 (solid grid)—and thus harder AGN ionizing radiation—in the direction of the black arrow. AM19 pure-shock (dashed) and shock+precursor (solid) model grids at varying velocities and magnetic fields are shown at different metallicities, with increasing values from lighter to darker green (following the green arrow). Shock models are more sensitive to the metallicity and have log([O III]/[O II]) $\gtrsim$0, but lower log([O I]/[O III]) ($\lesssim$0) than shock+precursor ones, which can reach log([O I]/[O III]) $\lesssim$1. The dashed-blue line qualitatively separates the SF from AGN/shock models, while the dashed–dotted-black line indicates the AGN locus. This plot represents a good tool to separate SF, AGN, and shock models for our sample, which includes subsolar to solar metallicity targets, underlining the importance of [O I] λ6300 as a good shock diagnostic at optical wavelengths. Only two CLASSY galaxies are at the edge of the star-forming locus. The galaxies with at least one UV emission line (i.e., C III] $\lambda\lambda$1907,9; 12 + log(O/H) $\lesssim$8.3) are highlighted by a thick black edge.

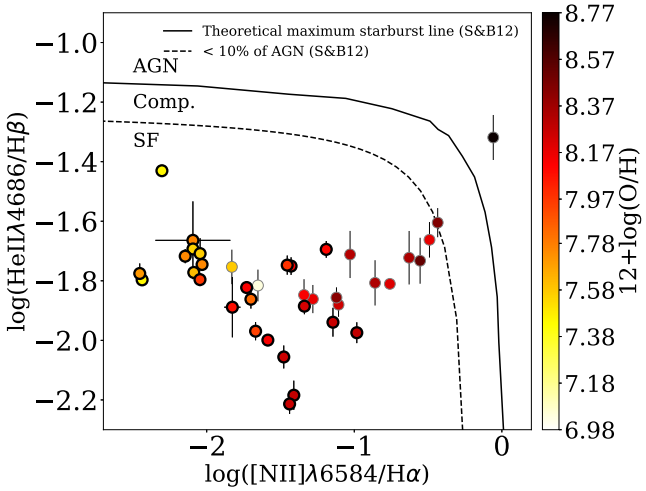

Figure 4. He II λ4686/Hβ vs. [N II]/Hα diagnostic diagram for the CLASSY galaxies, shown as dots, color coded as a function of the gas-phase metallicity. Only the measurements with S/N > 3 for all the lines involved are reported. The dotted- and solid-black lines represent the locus where $\sim$10% of He II λ4686 comes from an AGN and the theoretical maximum starburst line, respectively, as defined by Shirazi & Brinchmann (2012). Only two CLASSY galaxies are outside the star-forming locus, but we note that their He II λ4686 lines are particularly faint (S/N $\lesssim$ 5), hence this classification is not reliable by itself. The galaxies with at least one UV emission line (i.e., C III] $\lambda\lambda$1907,9; 12 + log(O/H) $\lesssim$8.3) are highlighted by a thick black edge.

The G16 models are not shown for clarity reasons but can completely cover the SF locus. Almost all of the CLASSY galaxies shown in the He II diagram are classified as star-forming. The only targets with a different classification are J0808+3948 (classified as AGN) and J1112+5503 (at the edge between the SF and composite locii). However, we emphasize that their He II lines are particularly faint (S/N $\sim$3–5), hence this classification is not reliable by itself. Given that J0808 +3948 is also not located in the SF locus in Figure 3 and in the [N II]–BPT (Figure 2), we conclude that it is possible that this galaxy has a further ionizing mechanism than pure SF. In Sections 4.1 and 4.2, we could not exclude the presence of shocks in our targets but, if present, shocks should easily enhance the He II λ4686 flux (e.g., Shirazi & Brinchmann 2012; Stasińska et al. 2015). However, here we stress that we do not see a particular enhancement of He II at increasing [O I]/[O III], which we consider a good shock diagnostic (Figure 3) or in galaxies where we identify a second broader component characterized by higher [N II]/Hα, [S II]/Hα, and/or [O I]/Hα, as shown and discussed in Figure 2. This is a further confirmation of the SF classification of our systems.

Finally, we highlight that almost all of the nine C III] $\lambda\lambda$1907 emitters are shown in Figure 4. The missing are: Izw 18 and J1253-0312, because they lack Hα measurement in our sample, but with log(He II λ4686/Hβ) ~ -1.35, -1.86 and 12 + log(O/H) $\sim$ 6.98, 8.06, respectively, and thus are still lying in the SF locus; Mrk 996 (J0127-0619) with an unreliable He II λ4686 flux measurement,

due to the contamination from the WR red clump, but still classified as star-forming (see James et al. 2009 for further details); and J1444+4237, which does not show He II λ4686 emission (upper limit of log(He II λ4686/Hβ) $\lesssim -1.8$), even though it has bright UV emission lines. Overall, all the galaxies that we will show in Section 5 are also classified as SF-dominated according to the Shirazi & Brinchmann (2012) criterion.

4.4. The Importance of Optical Coronal Lines

As a concluding note on optical diagnostics, we discuss the so-called coronal lines as proof of the presence of AGN activity. These are high-ionization (⩾70 eV) forbidden transitions excited by collisions similarly to [O III] λ5007 and are usually considered undeniable evidence of AGN ionization (e.g., Korista & Ferland 1989). Their presence in the optical (and IR) spectra of low-massive metal-poor galaxies is a currently intensively discussed issue in the hunt to reveal intermediate-mass black holes (e.g., Cann et al. 2020, 2021; Molina et al. 2021).

After a careful analysis of our spectra, we exclude the presence of these lines (i.e., [Fe VI] λ5146, [Fe XIV] λ5303, [Fe VII] λ5721, [Fe VII] λ6087, [Fe X] λ6374) in the optical spectra that we analyzed.[42] In the upper panel of Figure 1, next to [O I] λ6364 there is a bump that could be interpreted as a tentative [Fe X] λ6374. However, this feature is more consistent with the Si II λ6371 (actually a multiplet, Si II λλ6348,71), which was previously identified in some CLASSY galaxies in high-resolution optical spectra (e.g., VLT/GIRAFFE SBS 0335-052 E spectrum; Izotov et al. 2006). These permitted Si II lines may have a fluorescent origin and be produced by absorption of the intense UV radiation (Grandi 1976; Izotov et al. 2001). The detection of very high-ionization emission lines could be an alternative channel to identify hidden AGN activity in dwarf galaxies, especially in the JWST era with rest-frame IR coverage (e.g., Cann et al. 2018). However, here we want to highlight that it can be easy to misidentify [Fe X] λ6374 and Si II λ6371 (see also Herenz et al. 2023).

In conclusion, we stress that none of our galaxies are uniformly classified as non-SF dominated by the optical diagnostics considered here. According to the classical BPT diagrams with the standard separators, a few galaxies are classified as Comp/AGN, as shown in Table 2, but never consistently, while they are all classified as SF dominated using the separators from X18, thus taking into account the gas-phase metallicity of each object (Section 4.1 and Figure 2). Only two objects (J0944+3442, classified as SF by all the other diagrams, and again J0808+3948; both without UV lines) fall in the non-SF locus according to the oxygen line ratios used as shock diagnostics (Section 4.2 and Figure 3), ruling out shock dominated emission. Finally, the absence or very weak He II λ4686 lines is another strong indication of the lack of a harder mechanism than SF, with all the galaxies but J0808+3948 (with trans-solar metallicity and no UV lines) classified as SF dominated according to the Shirazi & Brinchmann diagram (Section 4.3 and Figure 4).

5. UV Diagnostic Diagrams

In the previous section, we showed how all the CLASSY galaxies characterized by UV emission lines are dominated by SF, using different optical criteria, highlighting all their caveats. Further confirmation of their SF-dominated nature lies in the lack of N V λλ1239,1243 doublet in emission. Indeed, in the UV, an unequivocal signature of AGN activity is generally represented by this very high-ionization emission doublet ($E > 77.5$ eV; Feltre et al. 2016). We do not observe the ISM N V doublet in emission in any of the CLASSY galaxies, but only in P-Cygni shape—strongly indicating the presence of massive stars (e.g., Chisholm et al. 2019). Having said that, here we want to explore if UV diagnostic diagram classification can be consistent with the optical, and thus identify the best-observed UV diagnostics to discriminate SF from AGN and shock ionization. Of course, without AGN within the sample, we are unable to assess the ability of UV diagnostics to correctly classify AGN, but we are able to test whether SF galaxies are incorrectly classified as AGN. We do this by comparing our sample of CLASSY galaxies with G16 constant and X18 BPASS bursty SF models, AM19 shock models, and F16 AGN models presented in Section 3 and Table 1. Furthermore, in Appendix C.1, we show and discuss G16 single-bursts and B17 models, also introduced in Section 3 and Table 1. As we introduced in Section 1, UV diagnostics can be crucial to investigate ISM properties with JWST observations in objects above $z \sim 6$, and thus it is important to understand in detail their strengths and drawbacks.

Specifically, in the following subsections, we show the UV diagnostic plots that we found more promising among those proposed in the literature on the basis of models and simulations (Feltre et al. 2016; Jaskot & Ravindranath 2016; Nakajima et al. 2018; Hirschmann et al. 2019, 2023):

1. C3He2–C4He2 (Figure 5): C III] λλ1907,9/He II λ1640 versus C IV λλ1549,51/He II λ1640;
2. C3He2–O3He2 (Figure 6): C III] λλ1907,9/He II λ1640 versus O III] λ1666/He II λ1640;
3. C4C3He2–C4C3 (Figure 7): C IV λλ1548,51/C III] λλ1907,9 versus (C IV+C III])/He II λ1640;
4. EWC4 and EWC3 (Figure 8): EW(C IV) and EW(C III]) versus C III]/He II λ1640.

We also report in Appendix C.2 the diagnostics diagrams C III]/He II λ1640 versus O III] λ1666/C III] λλ1907,9 (C3He2–O3C3) and C III]/He II λ1640 versus C IV λλ1548,51/C III] λλ1907,9 (C3He2–C4C3). Here we highlight that C IV and He II lines are broadly used in these diagrams, but they can have both a nebular and stellar contribution. We discuss this caveat in detail in Section 6.2.

As a general note about the AM19 shock grids, in all the following plots they are often completely overlapped in terms of velocity and magnetic field and gas-phase metallicity, but we decided to show the entire range of the v and B parameter space at three representative values of metallicity ($Z = 0.05$, 0.5, 1 $Z_{\odot}$) for completeness. These grids also cover very narrow regions in C4He2 space that correspond to the lowest velocities in the parameter space ($v < 200$ km s^{-1}, seen as spike-shaped features in grid coverage).

5.1. C3He2–C4He2

Figure 5 shows the C III] λλ1907,9/He II λ1640 versus the C IV λλ1548,51/He II λ1640 diagnostic diagram (C3He2–C4He2) with previously described SF, shock, and AGN grid models overlaid (see caption for details). This diagnostic diagram was first proposed as a good AGN and star-forming

[42] J0944-0038 MUSE data recently presented in del Valle-Espinosa et al. (2023) reveal [Fe VI] λ5146 line in the brightest SF knot, only partly covered by the SDSS and LBT data that we took into account.

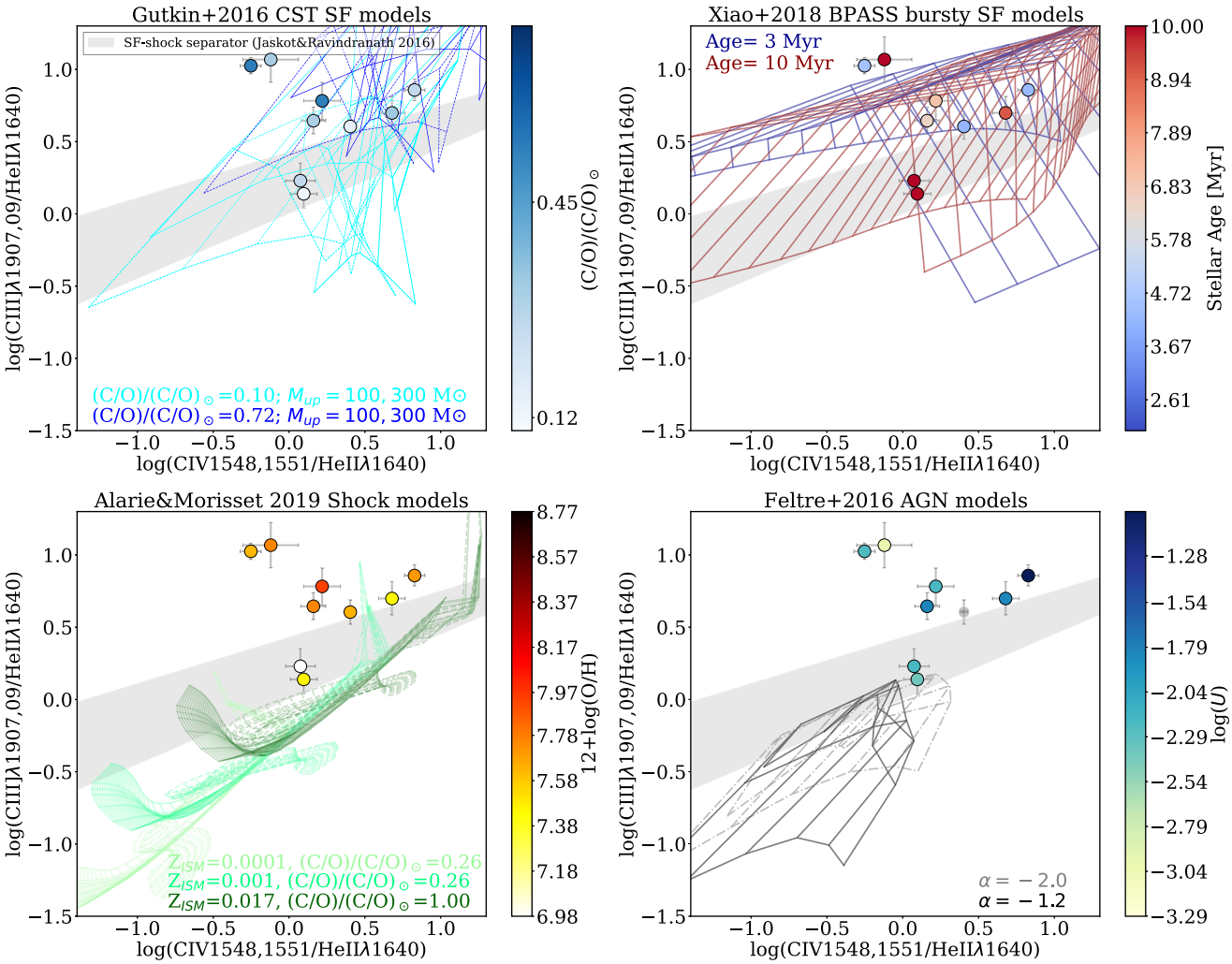

Figure 5. C3He2–C4He2 diagram: C III] $\lambda\lambda$1907,9/He II λ1640 vs. C IV $\lambda\lambda$1549,51/He II λ1640 diagnostic plot (F16, Jaskot & Ravindranath 2016) to separate SF and AGN activities. Here we show only the CLASSY galaxies with C IV detected in pure emission. The gray-shaded region represents the separator proposed by Jaskot & Ravindranath (2016) between pure-SF models (located above) and models with $\geqslant$50% shock contribution (located below). Upper left-hand panel: G16 models with continuous SF are shown in light ($(C/O)/(C/O)_{\odot} = 0.1$) and dark blue ($(C/O)/(C/O)_{\odot} = 0.72$), with the scatter plot color coded as a function of the $(C/O)/(C/O)_{\odot}$ measured for the sample. The solid and dashed grids refer to different IMF cut ($M_{up} = 100\ M_{\odot}$ and $M_{up} = 300\ M_{\odot}$, respectively). Upper right-hand panel: X18 models with burst of SF at 3 Myr and 10 Myr are shown in blue and red, respectively, with the scatter plot color coded as a function of the stellar age derived from the UV stellar-component fitting. Lower left-hand panel: AM19 shock models with increasing metallicities from light to dark green, as shown in the legend, and $(C/O)/(C/O)_{\odot} = 0.26$ are shown on a scatter plot color coded as a function of the gas-phase metallicity 12 + log(O/H) (darker green means higher metallicity, up to the trans-solar value of $Z_{ISM} = 0.017$). Lower right-hand panel: F16 AGN models with $\alpha = -2$ (solid − softer ionization) and $\alpha = -1.2$ (dashed–dotted - harder ionization) overplotted on a scatter plot color coded as a function of the ionization parameter log(U). The two galaxies located in the gray-shaded region are I Zw 18 and SBS 0335-052 E, which have the lowest 12 + log(O/H) and C/O abundance in the sample. Overall, the C3He2–C4He2 diagram can be used to discriminate SF from AGN and shocks, with some caveats. Shocks and AGN are harder to discriminate, but the former are still expected to have higher carbon-to-helium line ratios, especially at increasing metallicity.

galaxies separator in F16. Jaskot & Ravindranath (2016) further supported this as a good diagnostic plot to discriminate between shocks and pure SF, where their pure photoionization models lie above the shaded gray region in Figure 5, while most of their models with a shock contribution of $\geqslant$10% and $\geqslant$50% to the shown line ratios fall within and below the gray-shaded region, respectively. Indeed, the He II λ1640 line can be enhanced by hard ionizing radiation with high-energy photons (>54.4 eV), which can be produced by either AGN or shocks, causing a decrement of C III] $\lambda\lambda$1907,9/He II λ1640 and C IV $\lambda\lambda$1548,51/He II λ1640. This also implies that the C3He2-C4He2 diagram cannot clearly distinguish between AGN and shocks. Indeed, looking at the bottom panels of Figure 5, shock and AGN grids cover a similar C III]/He II versus C IV/He II parameter space, with the most metal-poor shock grids reaching C III]/He II and C IV/He II down to ~ -1.75 and ~ -2.5, respectively, as the $\alpha = -1.2$ AGN models (hardest AGN radiation) at the lowest values of metallicity and ionization parameter. Indeed, the strength of C III] and C IV is known to drop at decreasing metallicity ($12 + \log(O/H) \lesssim 7.5$; e.g., Jaskot & Ravindranath 2016; see also Paper IV) and decreasing C/O. We also notice that the AM19 shock models shown in Figure 5 can reach higher values than F16 AGN models in terms of C III]/He II line ratios, going beyond the gray-shaded SF-shock separator region at low values of velocities ($v < 200$ km s^{-1}, spike-shaped feature in the shown grids; see also Jaskot & Ravindranath 2016 Section 4.4).

The scatter plots in Figure 5, color coded as reported in the color bar labels, show the nine galaxies of our sample with

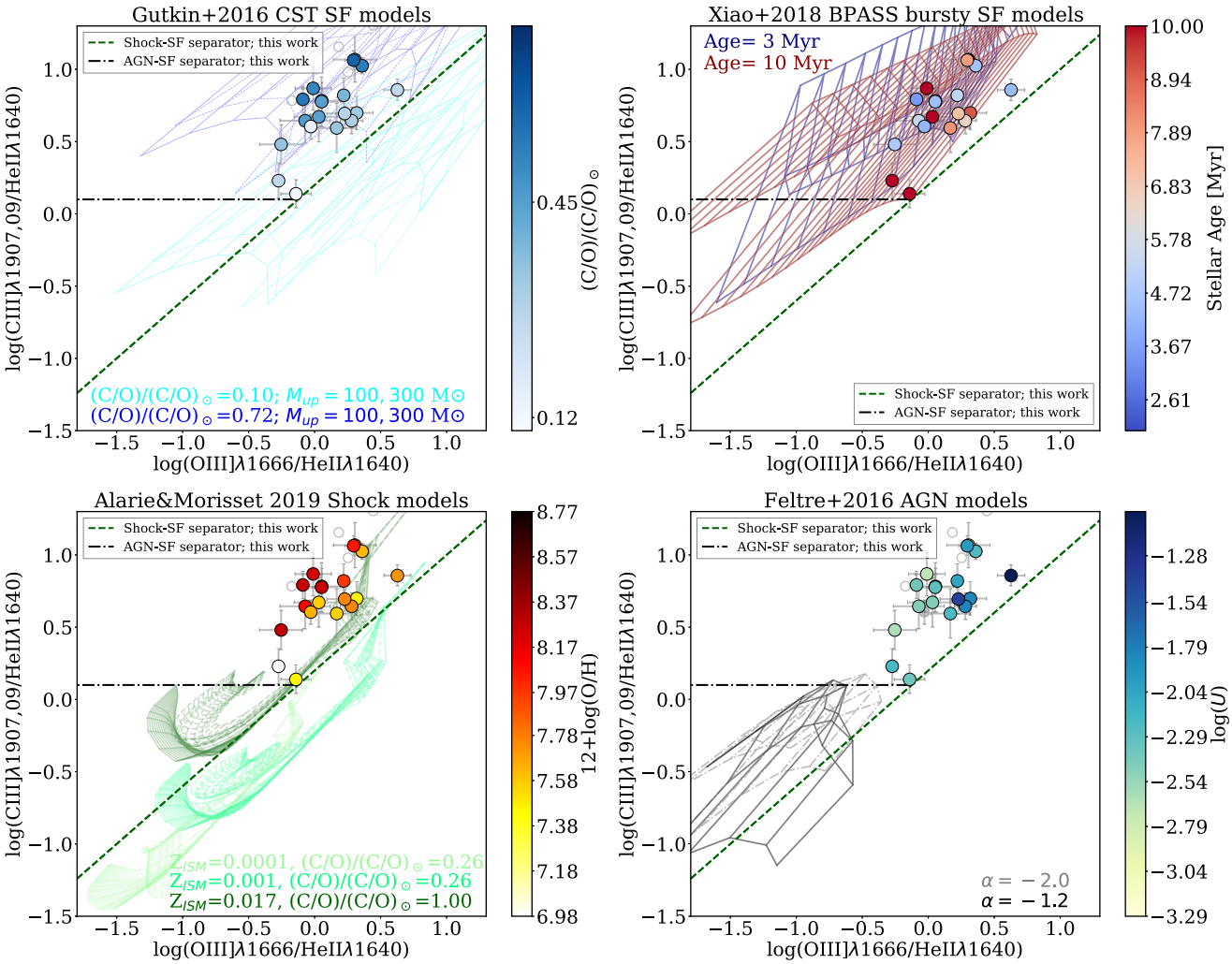

Figure 6. C3He2–O3He2 diagram: C III] λλ1907,9/He II λ1640 vs. O III] λ1666/He II λ1640 diagnostic diagram, proposed by F16. The filled and open dots show S/N > 3 and S/N < 3 fluxes for all the emission lines taken into account, respectively. The models superimposed are as explained in Figure 5. Overall, this represents the best diagram to discriminate SF, AGN, and shocks at subsolar metallicities (i.e., excluding the dark-green shock grid), due to the minimal overlap between each set of grids and the fact that all CLASSY galaxies are correctly classified as star-forming, as shown by the dashed-green and dashed–dotted lines to separate shock and AGN models from the SF locus (Equations (3) and (4)), respectively.

C IV λλ1548,51 in pure emission (the other galaxies show pure absorption or P-Cygni profiles). In particular, SBS 0335-052 E (J0337-0502) and I Zw 18 (J0934+5514) are located in the gray-shaded region that separates the pure-SF and shock locii according to Jaskot & Ravindranath (2016). Moreover, the two objects partially overlap with the F16 AGN models. However, from the optical diagnostics, we know that these galaxies are SF-dominated (Section 4). Interestingly, these objects are the two lowest metallicity galaxies of the sample showing UV emission lines ($12+\log(O/H)\sim7.46$ and ~6.98, respectively) with also the lowest C/O abundances ($(C/O)/(C/O)_{\odot}\sim0.26$ and ~0.12, respectively). This means that the Jaskot & Ravindranath (2016) criterion can fail in classifying extremely metal-poor star-forming objects possibly characterized by very hard ionization and low C/O, which could mimic AGN or shock ionization (see also Maseda et al. 2017). In agreement with this, G16 SF models (both CST and SSP) can fall beyond the Jaskot & Ravindranath (2016) pure-SF line when considering low C/O (cyan grids have $(C/O)/(C/O)_{\odot}=0.1$), which would reduce C III] and C IV emission. Another factor that pushes the G16 SF models below the Jaskot & Ravindranath (2016) pure-SF locus is a higher IMF upper-cut ($M_{up}=300\ M_{\odot}$ instead of $M_{up}=100\ M_{\odot}$, dashed and solid lines, respectively), which would imply more massive stars, and hence a harder ionization field (i.e., higher He II emission). Concerning G16 single-burst SF grids (that we do not show for clarity reasons but see Figure 13), only ages younger than ∼4 Myr can reproduce the line ratios observed for the CLASSY galaxies. Since the G16 models do not take into account either stellar rotation or binary interactions (which would amplify the galaxies ionizing fluxes for several Myr after a SF burst), the ionizing photons drop at older ages than 4 Myr, with subsequent reduction of He II (but also C III] and C IV), inducing a shift of the grids to higher C III]/He II and C IV/He II than the range shown in Figure 5 (see Appendix C.1 and e.g., Jaskot & Ravindranath 2016 Section 3.1 for a detailed comparison between different model prescriptions). In BPASS models, the stellar multiplicity instead impacts the duration of the ionizing photon production (as well as in B17 models that take into account stellar rotation; see Figure 13). Indeed, both the BPASS 3 Myr and 10 Myr star-forming grids of X18 can fully cover the CLASSY data and the SF locus in Figure 5, only slightly overlapping with the AM19 shock models.

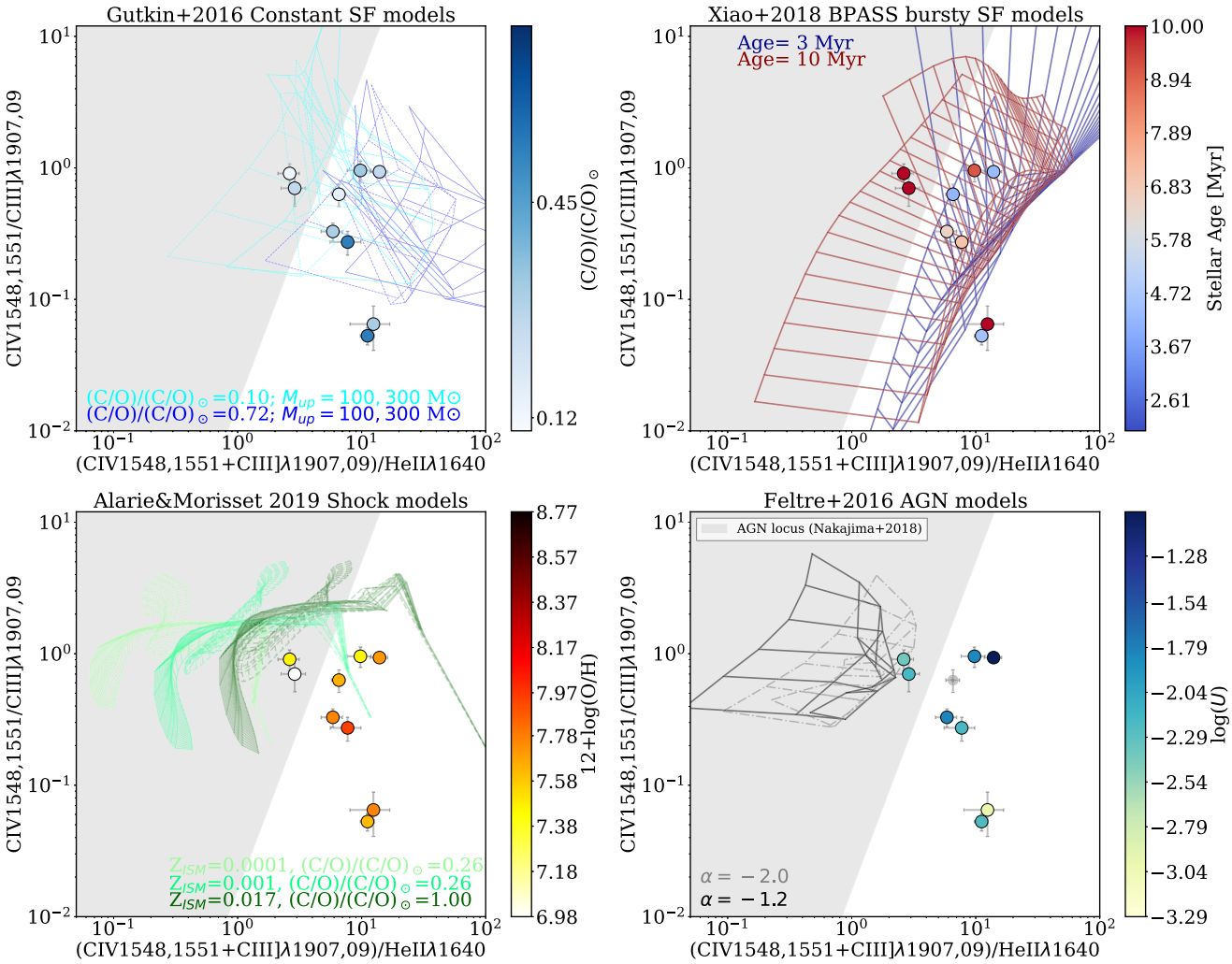

Figure 7. C4C3He2–C4C3 diagram: (C IV λλ1548,51+C III] λλ1907,9)/He II λ1640 vs C IV/C III] diagnostic plot proposed by Nakajima et al. (2018) to separate SF and AGN activities, with their proposed AGN-dominated region highlighted in shaded gray. The models superimposed are as explained in Figure 5. Similarly to Figure 5, this plot can be used to separate SF from AGN with some caveats. Indeed, the two galaxies which end up in the AGN locus are again I Zw 18 and SBS 0335-052 E, the two lowest 12 + log(O/H) and C/O abundance galaxies of the CLASSY sample, and can be reproduced by the low C/O SF grids (in cyan).

Overall, to explain the locations of galaxies such as SBS 0335-052 E and I Zw 18, lying in the region separating SF from harder mechanisms, the most likely explanation is their low O/H and C/O abundances (see also Wofford et al. 2021 for SBS 0335-052 E). Hence, before using the C3He2-C4He2 diagram the user should be mindful of the metallicity and C/O abundance of the targets, in that ionization sources in low-metallicity objects are less easily distinguishable for this diagnostic.

5.2. C3He2-O3He2

In Figure 6 we show the C III] λλ1907,9/He II λ1640 vs. O III] λ1666/He II λ1640 diagnostic diagram, proposed by F16 and further explored by Hirschmann et al. (2023). In contrast to the C3He2-C4He2 diagram shown in Figure 5, C3He2-O3He2 in Figure 6 can separate all of the three contributions of SF, AGN, and shocks quite well. This is with the exception of the G16 SF models with either low C/O or high M_{up} (both with constant and bursty SF), which, again, cover the entirety of the parameter space (see Section 5.1), as we further comment below. Most importantly, AGN and shock grids are only slightly overlapped, considering subsolar metallicities (considering $(C/O)/(C/O)_{\odot} = 0.26$), with shock models showing higher O III]/He II line ratios than AGN grids. Instead, the dark-green grid at trans-solar metallicity ($Z_{ISM} = 0.017$; $(C/O)/(C/O)_{\odot} = 1$) shifts to higher C III]/He II, overlapping more with the AGN and SF grids. In particular, He II emission is expected to increase in both AGN and shock models, as already discussed in Section 5.1, explaining the shift of AGN and shocks to lower C III]/He II and O III]/He II than SF grids (but $v < 200$ km s^{-1} shock models—spike-shaped in the shown grids—can reach C III]/He II comparable to SF grids as in Figure 5). However, shocks are also expected to have an increase of C III], which generally tightly correlates with temperature-sensitive lines such as O III] λ1666 (see e.g., Jaskot & Ravindranath 2016 Figures 12 and 9). This could explain the higher [O III]/He II for shocks than AGN models. As a reference, in Figure 6 we added a dashed-green line to separate shock models from the SF locus

$$y = 0.8\,x + 0.2 \quad (3)$$

and a horizontal dashed–dotted line to separate AGN models from the SF locus

$$y = 0.1 \quad \text{and} \quad -1.8 < x < -0.15 \quad (4)$$

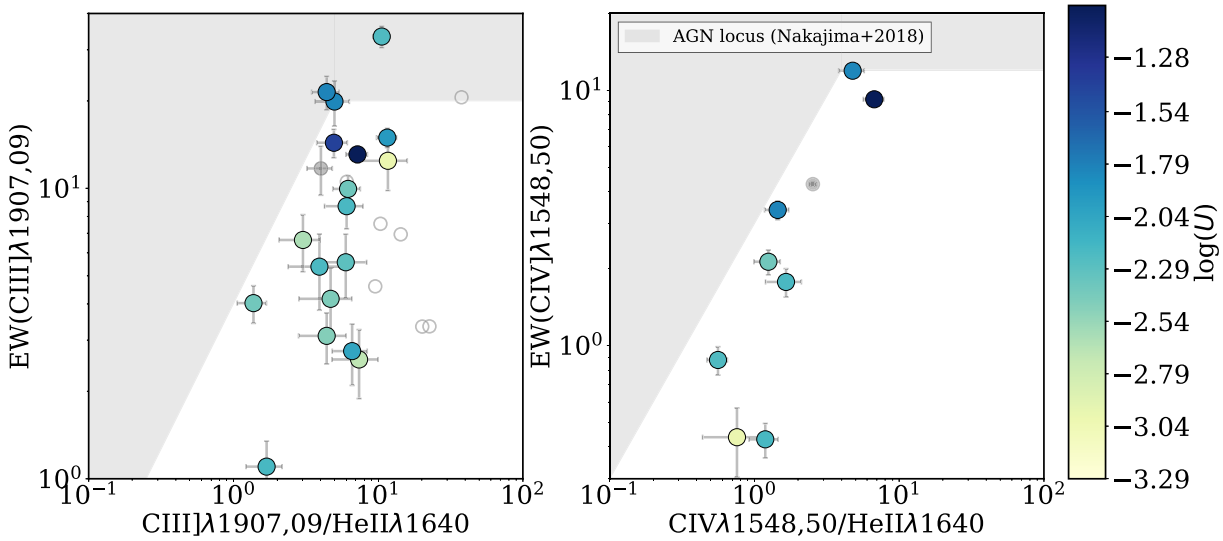

Figure 8. EW(C III]) and EW(C IV) diagnostic plots, where the gray-shaded regions represent the Nakajima et al. (2018) AGN locus, separated from the SF locus. The filled and open dots show S/N > 3 and S/N < 3 fluxes for all the emission lines taken into account, respectively. Interestingly, this classification scheme works well for the CLASSY galaxies, even for the most metal-poor systems.

with $x = \log(\text{O III}]\ \lambda1666/\text{He II}\ \lambda1640)$ and $y = \log(\text{C III}]\ \lambda\lambda1907{,}9/\text{He II}\ \lambda1640)$. The AGN grids again extend beyond the shown x- and y-ranges, with log(O III]/He II) and log(C III]/He II) down to ~ -1.5 and ~ -2.5, respectively, at the highest values of metallicity and lowest of ionization parameter.

The scatter plot in Figure 6 shows the 19 CLASSY galaxies with all the involved UV emission lines with S/N > 3. Interestingly, the parameter space covered by the CLASSY galaxies in this diagnostic diagram is very similar to that of the $z \sim 2$–4 galaxies of Nanayakkara et al. (2019), which further supports the classification of these systems as analogs to high-z SF galaxies. As in Figure 5, G16 SF models cover the majority of the C3He2-O3He2 plane. We notice that grids with low C/O abundances (solid- and dashed-cyan G16 grids in the upper left-hand panel) are shifted to lower C III]/He II and higher O III]/He II (trend in agreement with the C/O color coding shown in Figure 6 upper left-hand panel). This is probably due to the fact that carbon is a key coolant in the nebula, and thus a lower C/O ratio raises the electron temperature—as commented in Jaskot & Ravindranath (2016), and demonstrated by the decrease in metallicity (which is color coded in the bottom left-hand panel) as O3He2 increases. Hence, the increased collisional excitation rate partially compensates for the reduced C abundance, preventing an extreme drop of the C III]/He II ratio, and possibly enhancing [O III] λ1666. As a result, the low C/O G16 grids (solid- and dashed-cyan, according to the different IMF cut) manage to cover the lowest C III]/He II and O III]/He IISBS 0335-052 E and I Zw 18. X18 BPASS models instead are more confined in the SF locus, with the lowest metallicity and ionization parameter points of the grid slightly covering the region that we define as the AGN locus (below the black dashed–dotted line and above the dashed-black line in Figure 6).

Hirschmann et al. (2019) also proposed line separators to classify the main ionization mechanisms for the C3He2-O3He2 diagnostic plot, obtained from synthetic emission-line ratios computed by coupling G16 and F16 models with high-resolution cosmological zoom-in simulations of massive galaxies. However, according to Hirschmann et al. (2019) AGN-Composite and Composite-SF separators (which we do not report in Figure 6 for clarity reasons), all the CLASSY galaxies would be classified as composite. Hirschmann et al. (2019) also compared their simulated galaxies with observations of AGN and star-forming galaxies, finding generally good agreement with their classification. However, the local and high-z low-metallicity galaxies that they overplotted to their diagnostic diagrams also ended up in the composite region. Hence, we conclude that the Hirschmann et al. (2019) composite region also hosts star-forming galaxies with more "extreme" high-z characteristics that are typical of our sample.

Overall, we conclude that C3He2–O3He2 represents a better diagnostic diagram than C3He2–C4He2 because it is able to clearly separate (up to solar metallicities) the different mechanisms, with AGN showing lower O III]/He II than shocks, while SF-dominated emission shows higher C III]/He II. Moreover, all the CLASSY galaxies, even the most metal-poor SBS 0335-052 E and I Zw 18, are covered by the SF grids and do not overlap with the AGN or shock grids.

5.3. C4C3He2–C4C3, EWC4, and EWC3

Figure 7 shows the (C IV+C III])/He II versus C IV/C III] diagnostic plot proposed by Nakajima et al. (2018), with their proposed AGN locus shown in shaded gray. As in Figure 5, SBS 0335-052 E and I Zw 18 end up in the AGN locus, overlapping slightly with the F16 AGN models. Analogously to what we commented in Section 5.1, their shift can be explained in terms of their low $12 + \log(\text{O/H})$ and low C/O abundance. In this figure, it is even clearer that only the G16 SF models (both CST and SSP) with low C/O (cyan grids) can cover this subset of CLASSY galaxies, excluding two outliers. A higher C/O abundance grid with a high-cut in the IMF (dashed-blue grids) lies close but does not cover the lowest (C IV+C III])/He II line ratios, while the higher C/O abundance grid with $M_{\rm up} = 100\ M_{\odot}$ (solid-blue grids) does not cover the CLASSY galaxies. Overall, an increase of C/O quickly pushes the G16 grids (also the bursty SF grids at ages below 4 Myr; see Figure 13) toward values of (C IV+C III])/He II that are higher than what we typically observe in our

sample. X18 BPASS models (as well as B17; see Figure 13) can well reproduce the observed CLASSY line ratios, with the 3 Myr grids confined in the Nakajima et al. (2018) SF locus and the 10 Myr grids slightly shifted on the gray-shaded area of Figure 7, reaching the lowest values of C IV+C III])/He II at decreasing metallicity and ionization parameter. Moreover, AGN and shock grids are almost entirely overlapped (apart from the most metal-poor shock models, characterized by the lowest (C IV+C III])/He II).

Nakajima et al. (2018) proposed two other additional diagnostic plots to separate SF and AGN activities, shown in Figure 8, with the CLASSY data color coded as a function of the ionization parameter log(U). In particular, we notice that EW(C III]) and EW(C IV) increase at higher log(U), and the C IV and C III] emissions are also higher with respect to He II. This is clearer in the right-hand panel since EW(C IV) provides a valid log(U) tracer as demonstrated in Paper IV. As in Figure 7, the AGN regions according to Nakajima et al. (2018) criteria are shown in shaded gray. Nakajima et al. (2018) computed AGN photoionization models, assuming a continuum underneath the line emission dominated by the accretion disk, commenting that this is an overestimate because it does not take the effects of dust attenuation into account (i.e., presence of the torus). In general, evaluating the continuum emission to compute EWs in shock and AGN models implies many arbitrary assumptions because the continuum can have a composite nature, coming from both the stellar component and the additional ionizing sources, as well as their intrinsic characteristics. For this reason, F16 and AM19 do not provide EWs for their models. Meanwhile, all of the displayed CLASSY galaxies are in the SF locus defined by Nakajima et al. (2018), with the exception of J0944-0038 in the left-hand panel, characterized by EW(C III]) ∼33 Å, which still lies in a region where both AGN and SF models could overlap. In addition, X18 BPASS models can predict the observed range of C III] and C IV EWs by only taking very young ages (1 Myr) into account, which are shifted at higher C III]/He II and C IV/He II. Thus, it could be that the continuum to compute the EWs in these models is overestimated. Interestingly, the EW values predicted by G16 single-burst SF models with ages younger than 4 Myr cover the Nakajima et al. (2018) SF locus, and thus the EW(C III]) and EW(C IV) values observed for the CLASSY galaxies, while the constant SF models hardly reproduce them. As also commented for Figure 6, CLASSY galaxies fall entirely in the region defined as composite in Hirschmann et al. (2019), confirming that star-forming objects with the characteristics of the CLASSY sample (and thus high-z analogs) could risk being misclassified according to their criteria. Overall, these diagrams could be useful tools to classify even metal-poor star-forming galaxies, but they cannot be used to separate AGN from shocks because it is not trivial to evaluate the continuum to compute EWs in shock and AGN models.

5.4. Summary

All of the UV diagnostic diagrams discussed in the previous subsections, with some caveats, can distinguish SF from AGN and shocks, while it is only possible to disentangle AGN from shocks by taking into account C III], He II and O III] emission lines. Here we summarize our main findings:

1. The C3He2–C4He2 diagram (Figure 5) from Jaskot & Ravindranath (2016) can be used to discriminate SF from AGN and shocks. However, the users should be mindful of the metallicity and C/O abundance of the targets, in that ionization sources in low-metallicity objects are less easily distinguishable for this diagnostic. Shocks and AGN are harder to discriminate, but the former are still expected to have higher carbon-to-helium line ratios than the latter, especially at increasing metallicity.
2. C3He2–O3He2, proposed by F16, is the only diagram that is able to separate all the three ionization mechanisms at subsolar metallicities (Figure 6 and Equations (3), (4)). In this plot, all the CLASSY galaxies, even the objects characterized by the lowest 12 + log(O/H) and C/O (i.e., SBS 0335-052 E and I Zw 18), are covered by the G16 SF models and do not overlap to the AGN or shock grids, which cover similar C III]/He II but different O III]/He II line ratios (lower for AGN, higher for shocks). Other diagnostic diagrams from F16 are C3He2-C3O3 and C3He2-C4C3 (Appendix B), with the former able to separate SF, AGN, and shocks as C3He2–O3He2 (Equations (C1), (C2)), while the latter can only separate SF from AGN and shocks (Equations (C3), (C4)).
3. The C4C3He2–C4C3 diagram (Figure 7) from Nakajima et al. (2018) is a good diagnostic plot to separate SF and AGN, with the caveat of taking into account 12 + log (O/H) and C/O, similarly to C3He2–C4He2. However, it is not possible to distinguish between AGN and shocks, for which O3He2–C3He2 and C3He2–C3O3 would be better suited.
4. Finally, EWC4–C3He2 and EWC3–C3He2 (Figure 8) from Nakajima et al. (2018) also provide good diagnostic plots to separate star-forming galaxies from objects characterized by non-photoionization mechanisms via the Nakajima et al. (2018) AGN-SF separator line. This diagnostic diagram holds true even at low metallicity, low C/O abundance, and high log(U), but does not allow the user to discriminate shocks from AGN models, given the difficulties in estimating the corresponding EWs.

6. Discussion

In Sections 4 and 5, we demonstrated that our galaxies are SF dominated according to optical diagnostics, and then explored the most promising UV diagnostic diagrams, highlighting each of their strengths and weaknesses. In the following, we discuss the practicality of the UV diagnostic diagrams in terms of the observability of UV emission lines shown in this work and possible caveats when using them as diagnostics, and conclude with a comment on UV emission lines currently observed with JWST at high-z. We do this for two reasons: (1) to provide guidance on whether or not these lines should be expected in proposed observations of certain targets and (2) to provide context on the properties of the target if the lines are detected in their observations. Indeed, UV emission lines are a powerful (and at increasing redshift also the only) tool to investigate ISM conditions in galaxies.

6.1. Conditions for UV Emission in High-z Analogs

In general, we confirmed that the main two conditions to have UV emission-line detections in CLASSY (i.e., C IV $\lambda\lambda$1548,51, He II λ1640, O III] $\lambda\lambda$1661,6, C III] $\lambda\lambda$1907,9) are low metallicity and high-ionization parameter, traced by the [O III]/[O II] line ratio (but also [O III]/Hβ). Indeed, we see no

C III] λλ1907,9 (and thus no other UV emission lines) in CLASSY galaxies with $12+\log(\mathrm{O/H}) \gtrsim 8.3$. Specifically, we do not observe C III] in the eight CLASSY galaxies at metallicity higher than this threshold, where EW(C III]) $\lesssim 2$ Å and $\log(U) \sim -2.9$. This is also the reason why C III]-emitting galaxies (highlighted by thick black edges in all the figures) are systematically shifted to lower $\log([\mathrm{N\,II}]/\mathrm{H}\alpha)$ ($\lesssim -1$) in Figures 2 and 4), with the lowest metallicity targets ($12+\log(\mathrm{O/H}) < 7.8$) also having higher $\log(\mathrm{He\,II}\ \lambda 4686/\mathrm{H}\beta)$ line ratios (~ -1.4 to -1.8). However, the trend between the EW of UV lines and metallicity is not linear because carbon lines in our galaxies can be suppressed at $12+\log(\mathrm{O/H}) < 7.5$ (see, e.g., Figure 15 in Paper IV) and at decreasing C/O (D. A. Berg et al. 2024, in preparation). As such, low-metallicity is not a sufficient condition to ensure the presence of UV emission lines. In fact, there are nine CLASSY galaxies at $12+\log(\mathrm{O/H}) < 8.3$ without UV emission lines. These objects also have median values of EW(C III]) $\lesssim 2$ Å and $\log(U) \sim -2.8$. Indeed, the EW of UV lines also slightly correlates with $\log(U)$, with a significant decrease of detected UV lines at $\log(U) \lesssim -2.5$ for our sample. This is also visible from Figures 2 to 3, in which C III]-emitters are clearly shifted to higher $\log([\mathrm{O\,III}]/\mathrm{H}\beta)$ (∼0.5–1) and higher $\log([\mathrm{O\,III}]/[\mathrm{O\,II}])$ (∼0.5–1.5). Overall, this finding is consistent to previous works in the nearby Universe (e.g., Heckman et al. 1998; Ravindranath et al. 2020), as well as at higher redshift (e.g., Shapley et al. 2003; Rigby et al. 2015; Du et al. 2017).

The physical reason why UV metal lines are mostly only visible at low metallicity is well-explained in Jaskot & Ravindranath (2016) (see their Section 3.2). In particular, a decrease in metallicity implies a harder stellar ionizing radiation and a higher temperature nebula, and thus a larger amount of ionizing photons and a larger collisional excitation rate, respectively. Indeed, the UV metal lines are collisionally excited with energy levels above the ground state of $E/k \sim 6.5$–8.3 eV ∼75,000–97,000 K, which is much higher than optical collisional lines that typically have $E/k \ll 70{,}000$ K (e.g., ∼7.5 eV ∼87,000 K for O III] λλ1661,6 versus ∼2.5 eV ∼30,000 K for [O III] λ5007 and ∼5.4 eV ∼62,000 K for [O III] λ4363; Osterbrock & Ferland 2006; Draine 2011). Specifically, C III] λλ1907,9 (the brightest and most common) has the lowest $E/k \sim 75{,}000$, while the less common C IV λλ1548,51 and N IV] λλ have the highest $E/k \sim 93{,}000$–$97{,}000$ K. Hence, the UV lines are extremely temperature sensitive in photoionized gas that can reach $T \sim 2\times10^4$ K in our systems (see also Paper IV), compensating for the lower ionic relative abundances. As discussed in previous works (e.g., Jaskot & Ravindranath 2016), dust attenuation, density, SFR, and stellar population characteristics (stellar age and metallicity) can also play a role in the presence or absence of these UV lines, but we find no clear correlations comparing the derived quantities for the CLASSY galaxies with their UV emission strengths.

6.2. Caveats in Using CIV and HeII

UV lines such as He II λ1640 and C IV λλ1548,51 can have both a stellar and nebular origin, with C IV also being a resonant line affected by radiation transfer effects (e.g., Steidel et al. 2016). For many CLASSY galaxies, we can confirm He II and C IV nebular origin thanks to the general consistency of their intrinsic velocity dispersion values with those of O III] λλ1661,6 ($\sigma \sim 50$ km s^{-1}; Figure 1 bottom panel).

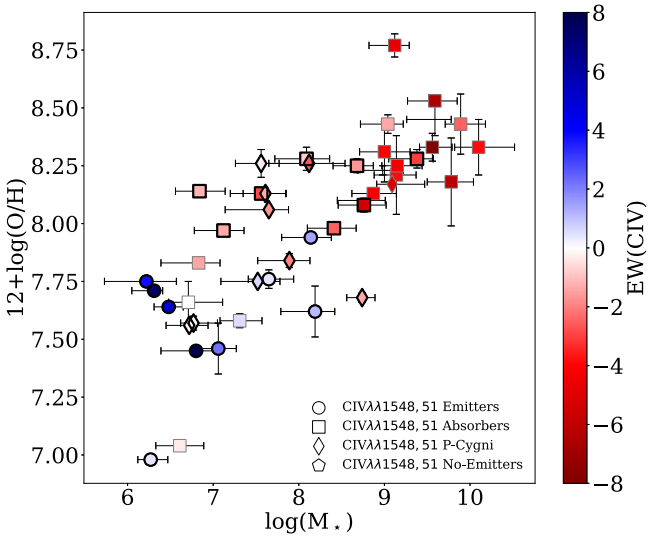

Figure 9. Mass-metallicity relation for CLASSY galaxies with C IV in emission (dots), absorption (squares), and P-Cygni (diamonds), color coded by EW(C IV), with red and blue values indicating negative (lines in absorption) and positive (lines in emission) EWs, respectively. The galaxies with at least one UV emission line (i.e., C III] are highlighted by a thick black edge. These plots show that galaxies which are C IV emitters, or with narrow P-Cygni non-stellar profiles, tend to have lower metallicities ($12+\log(\mathrm{O/H}) \lesssim 8$, 8.2) and lower stellar masses ($\log(M\star/M_\odot) \lesssim 8$, 9).

Concerning C IV, typical galaxies without an AGN show either C IV in absorption from the surrounding ISM or circumgalactic medium (CGM) gas or a P-Cygni profile from the stellar winds of massive stars (e.g., Leitherer et al. 2001). Nebular C IV emission is rarely observed in the literature, and comes uniquely from studies of systems with $12+\log(\mathrm{O/H}) \lesssim 8$ and generally high-ionization parameter $\log(U) \gtrsim -2.5$ (see Figure 16 in Paper IV), probably tracing a rapid hardening of the ionizing spectrum at low metallicities (see also Senchyna et al. 2019; Berg et al. 2021; Schaerer et al. 2022). From a visual inspection of C IV feature, we classified the CLASSY galaxies as being either C IV emitters (nine objects), P-Cygni (10), without C IV coverage (three), and defining the remaining others as ISM absorbers (23). Specifically, we applied the classification after normalizing for the stellar component, thus we only consider the ISM contribution of C IV doublet. We then calculated the EW(C IV) by integrating the C IV emission in a ∼10 Å window centered on the C IV lines, and the continuum in two featureless ∼5 Å windows on each side. We show the results of this exercise in Figure 9, where we color code the CLASSY mass–metallicity relation as a function of EW(C IV). In addition, galaxies with different C IV profiles are indicated using different symbols, as listed in the legend. Hence, within the CLASSY sample, C IV emitters (but also P-Cygni) are found to be more metal-poor and low-mass ($12+\log(\mathrm{O/H}) \lesssim 8$, 8.25 and $\log(M\star/M_\odot) \lesssim 8$, 9, respectively). It should be noted here, that the P-Cygni profiles here are very narrow and non-stellar (i.e., the stellar component has been subtracted) and should not be confused with the strong stellar P-Cygni profiles seen at high-metallicity. Meanwhile, C IV absorbers within the CLASSY sample have increasing EWs at larger stellar masses and metallicities. We do not find further particular correlations with other gas and stellar properties (e.g., SFR, $E(B-V)$, density). Of course, these inferences are being drawn from our local sample of high-z analogs and may not

hold true at all redshifts. Finally, we highlight that C IV is a resonant transition, meaning that high-ionization gas can scatter the photons. As discussed in Berg et al. (2019), resonantly scattered C IV emission appears broader than non-resonant emission lines (e.g., O III] λ1666) and double-peaked, as is usually found in Lyα studies (e.g., Hayes 2015; Verhamme et al. 2017; see also CLASSY Paper VII). In particular, Berg et al. (2019) confirmed this C IV resonant emission in two CLASSY galaxies, J1044+0353 and J1418+2102, which are the two objects that show the largest difference between C IV and O III] widths. The other CLASSY galaxies showing C IV in emission do not show the clearly double-peaked signatures (see Figure 2 in Paper IV) and have consistent values of σ(C IV) and σ(O III]).

Overall, given the complex nature of the C IV nebular emission (see also Section 6.4.1. of Paper IV), diagnostic diagrams involving the C IV lines (i.e., C IV/He II and C IV/C III] line ratios, as well as EW(C IV)) should be used with caution. The complexity of this line is also evident in the velocity offset that we find for C IV lines because they are systematically redshifted by ~25–100 km s^{-1} with respect to the other UV lines (see Figure 11 in Appendix A). This is also seen in Berg et al. (2019), Wofford et al. (2021), and could be consistent with resonance lines in an outflowing medium. Indeed, we found that to properly fit the C IV lines, we have to employ a different value of their velocity[43] (and thus line center) with respect to He II and O III]. However, to fully explore and compare in detail the different line kinematics, we would need integral-field spectroscopy data in the UV to see how the spectra change as a function of the location within the galaxy.

Moving to He II instead, its stellar contribution can be due to massive and very massive stars, including O-type stars and WRs, as commented in Section 1. A typical signature of stellar He II is a very broad width (e.g., Sixtos et al. 2023; Smith et al. 2023; Wofford et al. 2023), that can be distinguished from nebular emission via a comparison with close emission lines not affected by stellar contamination (i.e., O III] $\lambda\lambda$1661,6). The contribution of WR stars is more evident in optical spectra, where the He II λ4686 line can be blended with several metal lines in the so-called "blue-bump" (Brinchmann et al. 2008). As discussed in Section 3.1.1 of Paper IV, our stellar-component fitting accounts for different prescriptions for the evolution and atmospheres of massive stars, better accounting for He II λ1640 stellar contribution than other modeling prescriptions (e.g., Senchyna et al. 2021). The best example is Mrk 996 (J0127-0619), as shown in Figure 10, which hosts a significant WR population (James et al. 2009) and a broad He II λ1640 feature ($\sigma > 100$ km s^{-1}), which is completely stellar according to the C&B stellar-component fit (dashed-blue line), without signs of nebular emission. Only four CLASSY galaxies (i.e., J1129+2034, J1253-0312, J1200+1343, J1314+3452; see Figure 22 of Paper IV) have S/N(He II) >3 and σ(He II) >100 km s^{-1} (up to 200 km s^{-1} and broader than σ(O III]1666)), indicating that a stellar contribution can still be present despite our subtraction of the stellar-component emission. After a visual inspection of their optical spectra, these four galaxies show the presence of the WR blue-bump.

Overall, we acknowledge that He II λ1640 (both for its stellar/nebular origin and high-ionization potential) can also be problematic to reproduce by photoionization models (e.g., Gutkin et al. 2016; Steidel et al. 2016; Nanayakkara et al. 2019). This led some authors (e.g., Feltre et al. 2016; Hirschmann et al. 2019) to propose UV diagnostic diagrams without He II, comparing C IV $\lambda\lambda$1549,51 and C III] $\lambda\lambda$1907,9 with other UV lines, such as N V $\lambda\lambda$1239, 1243, N IV] $\lambda\lambda$1483,87 and N III] $\lambda\lambda$1747-54, or optical lines, such as [O III] λ5007 and [O I] λ6300 (that can be a good low-metallicity AGN and shock diagnostic, Section 4.1, 4.2). However, as shown in Paper IV, these UV lines, as well as Si III] $\lambda\lambda$1893,92, are very faint and observable in a handful of objects, while it is difficult to have extended coverage from the UV up to the very faint [O I] λ6300. This is the reason why we have not explored further UV diagnostic diagrams in this paper.

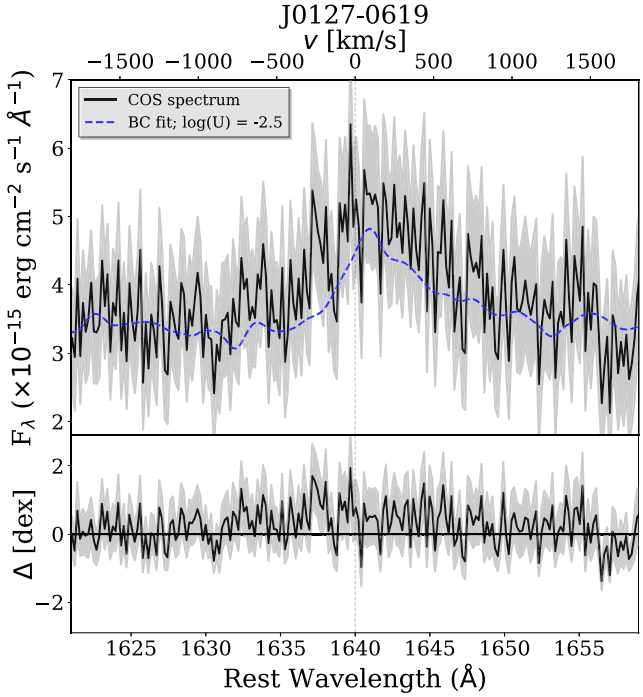

Figure 10. The He II λ1640 feature of Mrk 996 (J0127-0619) superimposed with the stellar-component best-fit made with C&B (dashed-blue line) described in detail in Section 3.1.1 of Paper IV. The bottom panel shows the difference between the observed spectrum and the C&B model. The very broad He II component ($\sigma > 100$ km s^{-1}) has a stellar origin, in contrast to the nebular He II emission that we generally observe in other CLASSY galaxies ($\sigma \sim 50$ km s^{-1}; see Figure 1 of this paper and also Figure 22 of Paper IV). This figure aims to illustrate the broad stellar He II profile and guide the user in its identification.

To conclude, we wish to highlight the advantages of detecting O III] $\lambda\lambda$1661,6 in UV spectra. As discussed in Paper IV, O III] is an auroral line like [O III] λ4363 and is thus sensitive to the gas temperature. It can be used to estimate C/O (see Section 2.1) and is more sensitive to shocks than carbon lines (Figure 6). Finally, the proximity of O III] to C IV and He II lines in UV spectra is useful for comparisons of the corresponding line widths to understand if the C IV and He II emission is purely nebular, as discussed in this subsection.

6.3. Current Observations of UV Emission Lines at High z

The UV diagnostics presented in this work and in CLASSY Paper IV can provide informative guidelines for interpreting high-z spectra. Such guidelines are especially important now that JWST has pushed the UV spectroscopic frontier to higher redshifts than ever before. Currently, large and deep JWST

[43] C IV lines were fitted separately from the other UV lines, as explained in Paper IV Section 3.2.

surveys, such as JADES, CEERS, and GLASS (e.g., Treu et al. 2022; Bunker et al. 2023a; Bagley et al. 2023), have started to provide statistically significant galaxy samples to study galaxy evolution from $z \sim 1$ until the epoch of reionization (up to $z \sim 13$). Up to now, the furthest spectroscopically confirmed galaxy is among the four young, metal-poor (stellar metallicity), and low-mass ($M \sim 10^7$–10^8 $M_\odot$) systems at $10.3 < z < 13.2$ presented in Curtis-Lake et al. (2023). Their redshifts were estimated using the Lyman-break as a reference because of the complete lack of both UV and optical emission lines. Indeed, so far, there has been a deficit in the amount of UV emission lines measured in the epoch of reionization. Despite becoming visible when stacking NIRSpec/prism spectra (using 38 JADES targets at $5 < z < 8$, priv. comm.), UV lines are detected in $\lesssim$4% objects in the latest JADES data release (Bunker et al. 2023a). This is puzzling given that pre-JWST ground-based rest-frame optical observations proved that galaxies at $z \sim 5$–7 show prominent high-ionization nebular-emission UV lines due to their extreme radiation fields and low metallicity (e.g., Stark et al. 2015; Mainali et al. 2017, 2018). The lack of observed UV emission lines in the current JWST observations could be due to a combination of several factors, such as the low spectral resolution ($R \sim 100$) of the NIRSpec prism (the most commonly used mode so far for wide-field MSA observations that is currently published), the reduced sensitivity of NIRSpec detector at shorter wavelengths, the depth of the exposures, or the physical conditions of the galaxies themselves. With regards to the galaxy conditions, metallicity in particular may not be the issue. Current observations are finding that high-z galaxies are generally metal-poor but not metal deficient, with metallicities of $Z \sim 0.03$–0.6 $Z_\odot$ (median $Z \sim 0.1$ $Z_\odot$ at $z \sim 3$–10; Curti et al. 2023), this range is comparable to the CLASSY sample. This suggests that UV lines are being produced in these systems, but not observed due to observational limitations.

The current furthest ($z \sim 10.603$) galaxy spectrum with clear UV and optical emission lines (from Lyα to Hγ) is GN-z11, which is the most luminous candidate $z > 10$ Lyman break galaxy in the GOODS-North field (Bunker et al. 2023b). Surprisingly, GN-z11 shows UV emission lines that we typically do not observe in CLASSY. Indeed, its NIRSpec/prism spectrum clearly shows both N IV] $\lambda\lambda$1483,7 and N III] λ1750 (Bunker et al. 2023b), which are very rarely observed in the local Universe (see Paper IV). This has opened an intense debate in the literature, with authors implying an extremely elevated nitrogen enrichment (at only 440 Myr from the Big Bang) and proposing different scenarios to explain it, including signatures of globular cluster precursors, massive star winds, runaway stellar collisions, or tidal disruption events (Senchyna et al. 2023b; Cameron et al. 2023; Charbonnel et al. 2023). Meanwhile, Maiolino et al. (2023) claimed that this object hosts AGN activity, which would be the origin of the peculiar nitrogen emission lines, thus solving the issue of the presence of the nitrogen lines and the puzzling N enrichment.

In particular, N IV] $\lambda\lambda$1483,7 lines (ionization potential $E > 47.5$ eV) are rarely seen in emission in SFGs (Fosbury et al. 2003; Raiter et al. 2010; Vanzella et al. 2010; Mingozzi et al. 2022; Harikane et al. 2024), trace very dense gas ($n_e > 10^4$–10^5 cm^{-3}), and (when present) they can also be (but not unambiguously) a signature of AGN ionization. N III] $\lambda\lambda$1750 is instead a multiplet that could have a nebular origin and be prominent in SFGs, but has been rarely observed (e.g., in the Sunburst Arc, a lensed $z \sim 2.4$ galaxy hosting a $\sim$3–4 Myr super star cluster; Pascale et al. 2023) and is visible in only two galaxies of the CLASSY sample: Mrk 996 (i.e., J0127-0619) and J1253-0312 (Figure 20 of Paper IV; log (N III] λ1750/He II λ1640) $\sim$1.34, 0.05, respectively), which are both also characterized by WR features in their optical spectra (as commented above). WR stars represent the best tracer of a young ongoing starburst in galaxies because they are uniquely characterized by very fast and strong winds (especially at high-metallicity), and thus a short lifetime ($\sim 10^5$ yr; Crowther 2007), that can lead to the production of prominent nitrogen features at both optical and UV wavelengths (e.g., Crowther & Smith 1997). In WR-dominated spectra, it is expected to also observe N IV] λ1719 resonance lines with a clear P-Cygni profile, which can help to discriminate between the nebular and stellar origin of the N III] and N IV] emission. The CLASSY galaxy Mrk 996 shows a N IV] λ1719 P-Cygni feature, a broad He II λ1640 (Figure 10), clear WR features in the optical spectra (James et al. 2009), and the N III] λ1750 multiplet, so a (partly) stellar origin of the UV N emission lines is plausible. In summary, the rare nature of nitrogen lines in UV spectra of nearby SFGs such as Mrk 996 could be due to the limited time frame of the starburst events that are causing them. To shed light on this and understand high-z galaxies such as GN-z11, we need further studies of local samples (including AGN galaxies) where we can broadly observe these UV nitrogen features to ultimately clarify their origin and diagnostic power. Taking into account all these considerations, at the moment we consider N lines to be unreliable diagnostics for the so-called UV BPT diagrams.

7. Conclusions

In this work, we investigated optical and UV diagnostics tracing different ionization mechanisms (i.e., SF, AGN, and shocks) using the CLASSY survey (Berg et al. 2022; James et al. 2022), which collects for the first time high-quality, high-resolution, and broad-wavelength-range FUV ($\sim$1200–2000 Å) spectra for 45 nearby ($0.002 < z < 0.182$) star-forming galaxies, including analogs of the high-z universe thanks to the broad ISM properties parameter space covered. This paper builds on our results shown in CLASSY Paper IV in which we measured CLASSY UV (from N IV] $\lambda\lambda$1483,7 to C III] $\lambda\lambda$1907, 9) and optical (from [O II] $\lambda\lambda$3727 to [S III] λ9069) emission lines, and several ISM properties (i.e., n_e, T_e, $E(B-V)$, $12 + \log(\mathrm{O/H})$, $\log(U)$).

As a first result of this paper, we are able to confirm the star-forming nature of our systems using well-known optical diagnostics that are sensitive to the dominant ionization source, while also taking into account their limitations due to the low metallicity of some of our galaxies. We then explored the proposed UV counterparts of these diagnostic diagrams—the so-called UV–BPT diagrams—from previous works based on photoionization and shock models (Gutkin et al. 2016; Jaskot & Ravindranath 2016; Hirschmann et al. 2019, 2023). To do this, we compared our measured line ratios (and their corresponding ISM properties) with a set of state-of-the-art models taken from the literature: constant and single-burst SF models from G16, AGN models from F16, and shock models from the 3MdBs[44] database (AM19). Finally, we discussed which conditions favor the detection of UV emission lines. In the following, we summarize our findings:

[44] http://3mdb.astro.unam.mx/

1. In Section 4, we explored the classical BPT diagrams, as well as the use of [O I] λ6300 as a shock diagnostic and the Shirazi & Brinchmann (2012) diagram, which takes the He II λ4686 emission line into account. In particular, we showed that CLASSY galaxies have [O III]/Hβ and He II λ4686/Hβ typical of SFGs. In addition, their broad components (if present) are still generally classified as star-forming and, even though have enhanced [N II]/Hα, [S II]/Hα, [O I]/Hα and [O I]/[O III] and low [O III]/[O II] (possible evidence of shocks), they do not correlate with He II λ4686, which could be enhanced by shock ionization. Overall, it is not possible to completely exclude the presence of shocks (and possibly AGN activity for the only trans-solar metallicity CLASSY galaxy) but the main ionizing mechanism is clearly SF, especially for the CLASSY subsample showing UV emission lines.
2. In Section 5, we presented our list of reliable UV diagnostic plots that we explored for the CLASSY galaxies showing UV emission lines. Many of the discussed UV diagnostic diagrams can separate SF from AGN and shocks, with the caveat that low $12+\log(\mathrm{O/H})$ and carbon abundance C/O objects can fall in the AGN/shock-locus proposed by previous authors (e.g., C3He2–C4He2, Figure 5; C4C3He2–C4C3, Figure 7; and C3He2–C4C3 in Appendix B), while they usually struggle in separating AGN from shocks. Diagnostics using carbon lines equivalent widths identify the SF locus, even at low metallicity, low C/O abundance, and high $\log(U)$ (e.g., EWC4–C3He2 and EWC3–C3He2; Figure 8), but the modeled EWs are heavily dependent on the model assumptions of the continuum component. In addition, the C IV doublet has a complex nature that still needs to be properly understood and is rarely observed to be purely nebular (see also Section 6), thus diagnostic diagrams to investigate the ionization source or ISM properties involving these lines should be used with caution.
3. In Section 5, we also concluded that the combination of C III] $\lambda\lambda$1907,9, He II λ1640 and O III] λ1666 (C3He2–O3He2, Figure 6, see Equations (3), (4); C3He2–C3O3 in Appendix B, Equations (C1), (C2)) represents the best diagnostic diagram to separate all the three ionization mechanisms at subsolar metallicities. In particular, AGN models show lower O III]/He II and O III]/C III] than shocks, while SF grids are usually located at higher C III]/He II than AGN and shocks.
4. In Section 6, we confirmed that UV emission lines observed in CLASSY (with C III] $\lambda\lambda$1907,9, the most common FUV line, excluding Lyα) are mainly favored in ISMs with low-metallicity and high-ionization parameters, with none of them visible in targets with $12+\log(\mathrm{O/H})\gtrsim 8.3$. In particular, C III]-emitters have systematically lower $\log([\mathrm{N\,II}]/\mathrm{H}\alpha)$ ($\lesssim -1$; see Figure 2), can reach high values $\log(\mathrm{He\,II}\ \lambda4686/\mathrm{H}\beta)$ (~ -1.4–1.8; Figure 4), and are clearly shifted to higher $\log([\mathrm{O\,III}]/\mathrm{H}\beta)$ ($\sim$0.5–1) and higher $\log([\mathrm{O\,III}]/[\mathrm{O\,II}])$ ($\sim$0.5–1.5; Figure 2), and thus higher $\log(U)$. We also describe the caveats involved with using C IV $\lambda\lambda$1548, 51 and He II λ1640 emission lines, and showed that those measured in CLASSY are mainly nebular, given the consistency of their velocity dispersion with O III] λ1666 ($\sigma\sim 50$ km s^{-1}; Figure 1). Finally, while reflecting on the currently puzzling detection of UV emission in high-z systems with JWST, we underlined the almost total absence of nitrogen UV lines (i.e., N IV] $\lambda\lambda$1483,7, N III] λ1750) in the CLASSY survey. Hence, we need further studies of samples where we can observe these features before attesting their reliability as diagnostics to investigate the main source of ionization.

Overall, this paper together with Paper IV uses the CLASSY survey to provide the toolkit to investigate ISM properties using UV emission lines. This can be particularly important to explore the $z>6$ rest-frame UV spectra in the JWST era, in which an unprecedented number of EoR galaxies have already been revealed (e.g., Arellano-Córdova et al. 2022a; Curti et al. 2022; Roberts-Borsani et al. 2022; Bunker et al. 2023b; Cameron et al. 2023; Curtis-Lake et al. 2023).

Acknowledgments

M.M., D.A.B., K.Z.A.-C., and X.X. are grateful for the support for this program, HST-GO-15840, that was provided by NASA through a grant from the Space Telescope Science Institute, which is operated by the Associations of Universities for Research in Astronomy, Incorporated, under NASA contract NAS5-26555. In addition, M.M. is grateful to Carlo Cannarozzo, Giovanni Cresci and Alessandro Marconi for inspiring conversations and advice. B. L.J., S.H., and N.K. are thankful for support from the European Space Agency (ESA). A.F. acknowledges the support from grant PRIN MIUR2017-20173ML3WW_001. A.W. acknowledges the support of UNAM via grant agreement PAPIIT no. IN106922. R. A. acknowledges support from ANID Fondecyt Regular 1202007. J.B. acknowledges support by Fundação para a Ciência e a Tecnologia (FCT) through the research grants UID/FIS/04434/2019, UIDB/04434/2020, UIDP/04434/2020, national funds PTDC/FIS-AST/4862/2020 and work contract 2020.03379.CEECIND.

The CLASSY collaboration extends special gratitude to the Lorentz Center for useful discussions during the "Characterizing Galaxies with Spectroscopy with a view for JWST" 2017 workshop that led to the formation of the CLASSY collaboration and survey. The CLASSY collaboration thanks the COS team for all their assistance and advice in the reduction of the COS data.

Funding for SDSS-III has been provided by the Alfred P. Sloan Foundation, the Participating Institutions, the National Science Foundation, and the U.S. Department of Energy Office of Science. The SDSS-III website is http://www.sdss3.org/. SDSS-III is managed by the Astrophysical Research Consortium for the Participating Institutions of the SDSS-III Collaboration including the University of Arizona, the Brazilian Participation Group, Brookhaven National Laboratory, Carnegie Mellon University, University of Florida, the French Participation Group, the German Participation Group, Harvard University, the Instituto de Astrofisica de Canarias, the Michigan State/Notre Dame/JINA Participation Group, Johns Hopkins University, Lawrence Berkeley National Laboratory, Max Planck Institute for Astrophysics, Max Planck Institute for Extraterrestrial Physics, New Mexico State University, New York University, Ohio State University, Pennsylvania State University, University of Portsmouth, Princeton University, the Spanish Participation Group, University of Tokyo, University of Utah, Vanderbilt University, University of Virginia, University of Washington, and Yale University.

This work also uses the services of the ESO Science Archive Facility, observations collected at the European Southern Observatory under ESO programs 096.B-0690, 0103.B-0531, 0103.D-0705, and 0104.D-0503, and observations obtained with the Large Binocular Telescope (LBT). The LBT is an international collaboration among institutions in the United States, Italy, and Germany. LBT Corporation partners are: The University of Arizona on behalf of the Arizona Board of Regents; Istituto Nazionale di Astrofisica, Italy; LBT Beteiligungsgesellschaft, Germany, representing the Max-Planck Society, The Leibniz Institute for Astrophysics Potsdam, and Heidelberg University; The Ohio State University, University of Notre Dame, University of Minnesota, and University of Virginia.

This research has made use of the HSLA database, developed and maintained at STScI, Baltimore, USA.

All of the HST data used in this paper can be found in MAST: doi:10.17909/m3fq-jj25.

Facilities: HST (COS), LBT (MODS), APO (SDSS), KECK (KCWI, ESI), VLT (MUSE, VIMOS)

Software: astropy (Astropy Collaboration et al. 2013, 2018, 2022) BEAGLE (Chevallard & Charlot 2016), CalCOS (STScI), dustmaps (Green 2018), jupyter (Kluyver et al. 2016), LINMIX (Kelly 2007), MPFIT (Markwardt 2009), MODS reduction Pipeline, Photutils (Bradley et al. 2021), PYNEB (Luridiana et al. 2012, 2015), python, pysynphot (STScI Development Team), RASCAS (Michel-Dansac et al. 2020), SALT (Scarlata & Panagia 2015), STARLIGHT (Fernandes et al. 2005), TLAC (Gronke & Dijkstra 2014), XIDL

Appendix A
Comparing UV and Optical Kinematics

Here we want to further discuss the emission-line kinematics, while also comparing optical and UV results. The left- and right-hand panels of Figure 11 show the velocity offset of the UV stellar (left-hand panel) and gas kinematics (right-hand panel) with respect to the systemic velocity v_{sys} (derived from z_{lit}), consistent with the ionized gas velocity measured from optical emission lines, as a function of the galaxy stellar mass. In general, we find no systematic offsets between the ionizing stellar-component velocity explored by fitting the UV spectra (magenta squares) and v_{sys}, with Δv mainly within $\pm\sim 50$ km s^{-1} and median value $\langle\Delta v\rangle\sim 7$ km s^{-1} (dashed–dotted-magenta line). One implication is that the narrow components of the optical emission lines are really tracing non-outflowing gas (Rigby et al. 2018). The right-hand panel of Figure 11 instead shows the O III] $\lambda\lambda$1661,6, C III] $\lambda\lambda$1907,9, and C IV $\lambda\lambda$1548,51 velocities as red dots, blue triangles and yellow stars. There is a scatter between the UV and systemic velocities mainly within $\pm\sim 50$ km s^{-1}, and more enhanced for some C III] measurements, with three galaxies (J1359+5726, J0926+4427 and J0942+3547) showing a clear redshifted offset ($\Delta v\sim +100$–200 km s^{-1}) and three (I Zw 18, Mrk 996 and J1025+3622) showing a clear blue-shifted offset ($\delta v\sim -150$–200 km s^{-1}). However, we do not see any systematic offsets, as shown by the dashed-red and dotted-blue lines indicating the corresponding median values with respect to v_{sys}. Hence, we conclude that it is unlikely that they are due to issues in the G185M grating calibration, covering the C III], discussed in detail in James et al. (2022).

Interestingly, we find a systematic offset between the v_{CIV} and v_{sys} with a median value of $\langle\Delta v\rangle\sim +60$ km s^{-1} (solid-gold line), implying that C IV emission is systematically redshifted with respect to the systemic velocity, consistently with resonant scattering/absorption (see also Berg et al. 2019; Wofford et al. 2021). For seven out of the nine galaxies for which we measure C IV nebular emission, this blue-shifted offset increases with the stellar mass, going from $\sim$0 km s^{-1} to $\sim$90 km s^{-1} in the range $\log(M_\star/M_\odot)$ 6–8. The two exceptions are I Zw 18 and J1323-0132, with stellar masses of $\log(M_\star/M_\odot)\sim$6.3, showing $\delta v\sim 65$ km s^{-1}.

As discussed in Section 2.2 and in Figure, 1, optical emission lines of half of the CLASSY sample needed a narrow and a broad Gaussian component to be accurately reproduced. Looking at the single and narrow component σ values shown in the right-hand panel of Figure, 1, we see that σ (and also its

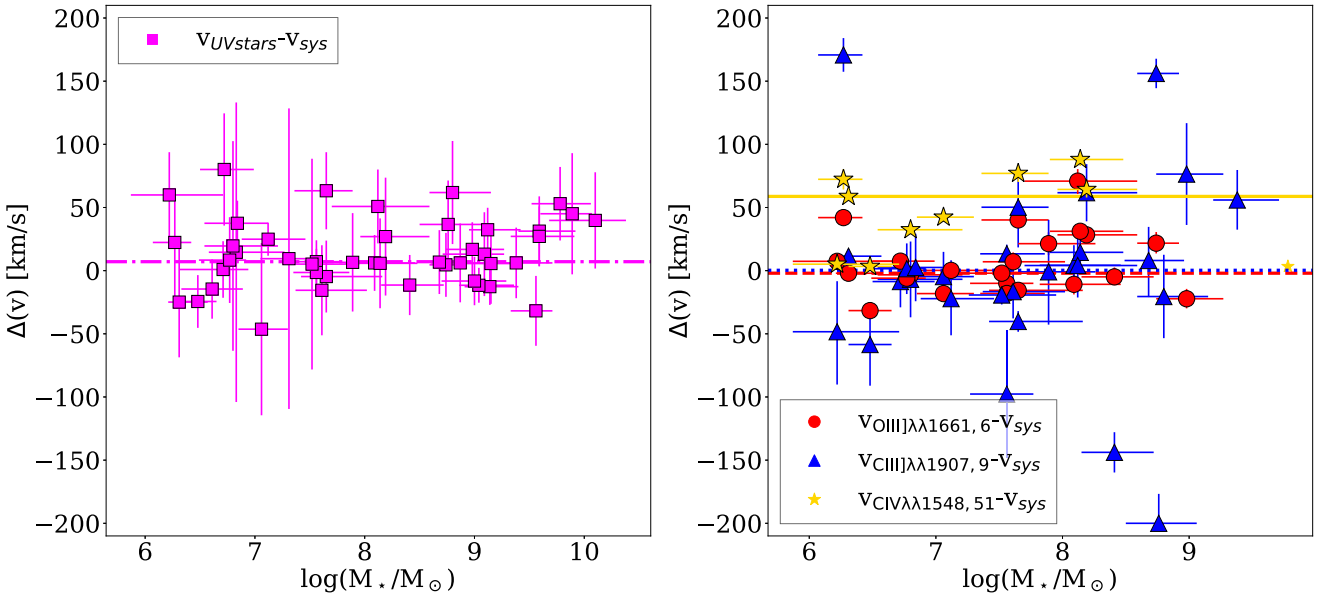

Figure 11. Velocity offset of the UV stellar (left-hand panel, magenta squares) and gas kinematics (right-hand panel) with respect to the systemic velocity v_{sys}, consistent with the ionized gas velocity measured from optical spectra, and as a function of the galaxy stellar mass. In the right-hand panel, we indicate the O III] $\lambda\lambda$1661,6, C III] $\lambda\lambda$1907,9, and C IV $\lambda\lambda$1548,51 velocities as red dots, blue triangles and yellow stars, as reported in the legend.

scatter) increases at larger stellar masses, with only objects with $M_\star \gtrsim 10^7\ M_\odot$ needing a two-component fit. We highlight here that all the galaxies characterized by a broad component in optical emission lines (apart Mrk 996 and SBS 0335-052 E) were found to have an outflowing component in rest-UV absorption lines analyzed by Xu et al. (2022, 2023) (CLASSY Paper III, Paper VI). Recent studies have shown that low-mass systems ($M_\star < 10^9\ M_\odot$) such as those of the CLASSY survey can have irregular velocity fields in the ionized gas studied through optical emission lines, indicating the presence of non-circular motions (e.g., Marasco et al. 2023). However, galactic winds, defined as gas at velocities larger than the galaxy escape speed, have been found to be able to account for only a few percent of their observed fluxes in both the local universe (Marasco et al. 2023) and at $z \sim 1.2$–2.6 (Concas et al. 2022). Here we highlight that the lack of galactic wind detection in small systems could be also an issue of S/N, but in this work we do not explore this topic any further, leaving it to a future study using optical integral-field spectroscopy data, that can provide both a spatial and kinematical information of our galaxies, and thus a more complete picture that the integrated optical spectra analyzed here cannot provide.

Appendix B
Alternative Diagnostic Diagrams

Figure 12 shows an alternative optical-diagnostic diagram to discriminate the excitation properties, using [O II] $\lambda\lambda$3727/Hβ versus [O III] λ5007/Hβ line ratios (Lamareille et al. 2004; Lamareille 2010). The dotted, solid, and dashed lines indicate the empirical dividing line between star-forming galaxies and AGN identified by Lamareille et al. (2004), while the dashed–dotted line identifies the empirical locus of LI(N)ER and composite galaxies, found by Lamareille (2010). The advantage of this diagram is that it can be used to explore JWST targets at redshifts up to $z \sim 8.5$ in the observed NIR (with

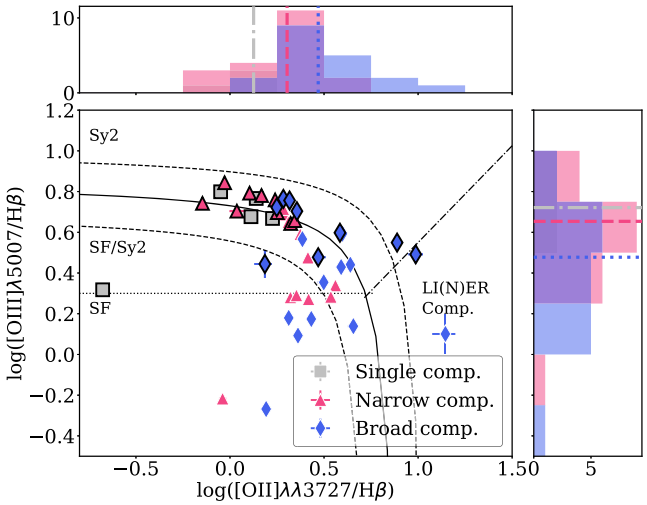

Figure 12. Analogously to Figure 2, [O II] $\lambda\lambda$3727/Hβ vs. [O III] λ5007/Hβ diagnostic diagram for the narrow and broad components of the CLASSY galaxies, shown as red dots and blue diamonds, respectively. Only the measurements with S/N > 3 for all the lines involved are reported. The dotted and solid lines indicate the empirical dividing line between star-forming galaxies and AGN identified by Lamareille et al. (2004), the dashed lines show the uncertainty region, while the dashed–dotted line identifies the empirical locus of LI(N)ER and Seyfert galaxies, found by Lamareille (2010). Unfortunately, this diagnostic plot does not represent a good tool to discriminate among the different ionizing mechanisms of our systems.

NIRISS or NIRspec), for which redder wavelengths are unavailable (e.g., Curti et al. 2022). However, this diagram should be taken with caution because, as shown in Table 2, it does not always disentangle ionizing mechanisms in our sample, with many galaxies (classified as star-forming according to the classical BPT) lying in the boundary region between SF and Seyferts, and thus classified as composite. This shows the limit of [O II]/Hβ in distinguishing among ionization mechanisms.

Appendix C
Other UV Diagnostic Diagrams

C.1. The Effect of Stellar Rotation and Multiplicity on UV Line Ratios

In this section, we compare G16, B17 and X18 bursty models presented in Table 1. B17 models only take stellar rotation into account and X18 models only take stellar multiplicity into account, while G16 models take neither of the two into account. The differences in how G16 and B17 grids differ with respect to X18 models in the UV diagnostic diagrams discussed in Figures 5, 6, and 7 are shown in Figure 13.

In Figure 13, we show G16 and B17 grids at 3, 5, and 10 Myr. The bursty G16 grids seem unable to reproduce the lowest C IV/He II, C III]/He II and (C IV+C III])/He II line ratios. This happens because, for clarity reasons, we have only shown a subset of G16 model parameter space, considering only $(C/O)/(C/O)_\odot = 0.72$ and the IMF cut at $M_{up} = 100\ M_\odot$. Considering either a lower C/O or a higher IMF cut, the 3 Myr grid can reproduce the line ratios observed for the CLASSY galaxies, as shown for the constant SF grids in Figures 5, 6, and 7. However, at higher ages, the ionizing photons drop with a subsequent reduction of He II (but also C III] and C IV), inducing a shift of the grids to higher C III]/He II and C IV/He II than the range shown in Figure 5 (see e.g., Jaskot & Ravindranath 2016 Section 3.1 for a detailed comparison between different model prescriptions). Meanwhile, B17 models at 3 and 5 Myr behave similarly to X18 grids at 3 and 10 Myr,[45] with the one at 5 Myr going beyond the SF locus defined by the CLASSY galaxies, partly covering the shock/AGN regions. The B17 grid at 10 Myr is, instead, unable to reproduce the observed line ratios, being shifted to higher C III]/He II and (C IV+C III])/He II (in the opposite direction with respect to the AGN/shock regions) because of the reduced ionizing radiation, and unable to enhance He II emission. The main take-away from Figure 13 is that, as discussed in Section 3, stellar rotation and multiplicity have the effect of amplifying the stellar ionizing radiation for several Myr after a SF burst. Overall, the different grids at 3 Myr can reproduce the observed line ratios of star-forming galaxies.

C.2. Other UV Diagnostic Diagrams

Figures 14 and 15 show the C3He2-C3O3 and C3He2-C4C3 diagrams, respectively, proposed together with the C3He2-O3He2 diagram (Figure 6) by F16. C3He2-C3O3 behaves similarly to C3He2-O3He2 (Figure 6), and thus, at subsolar metallicities, it can clearly distinguish among SF, AGN, and

[45] X18 grids at 5 Myr are not shown in this paper, but are consistent with those at 10 Myr.

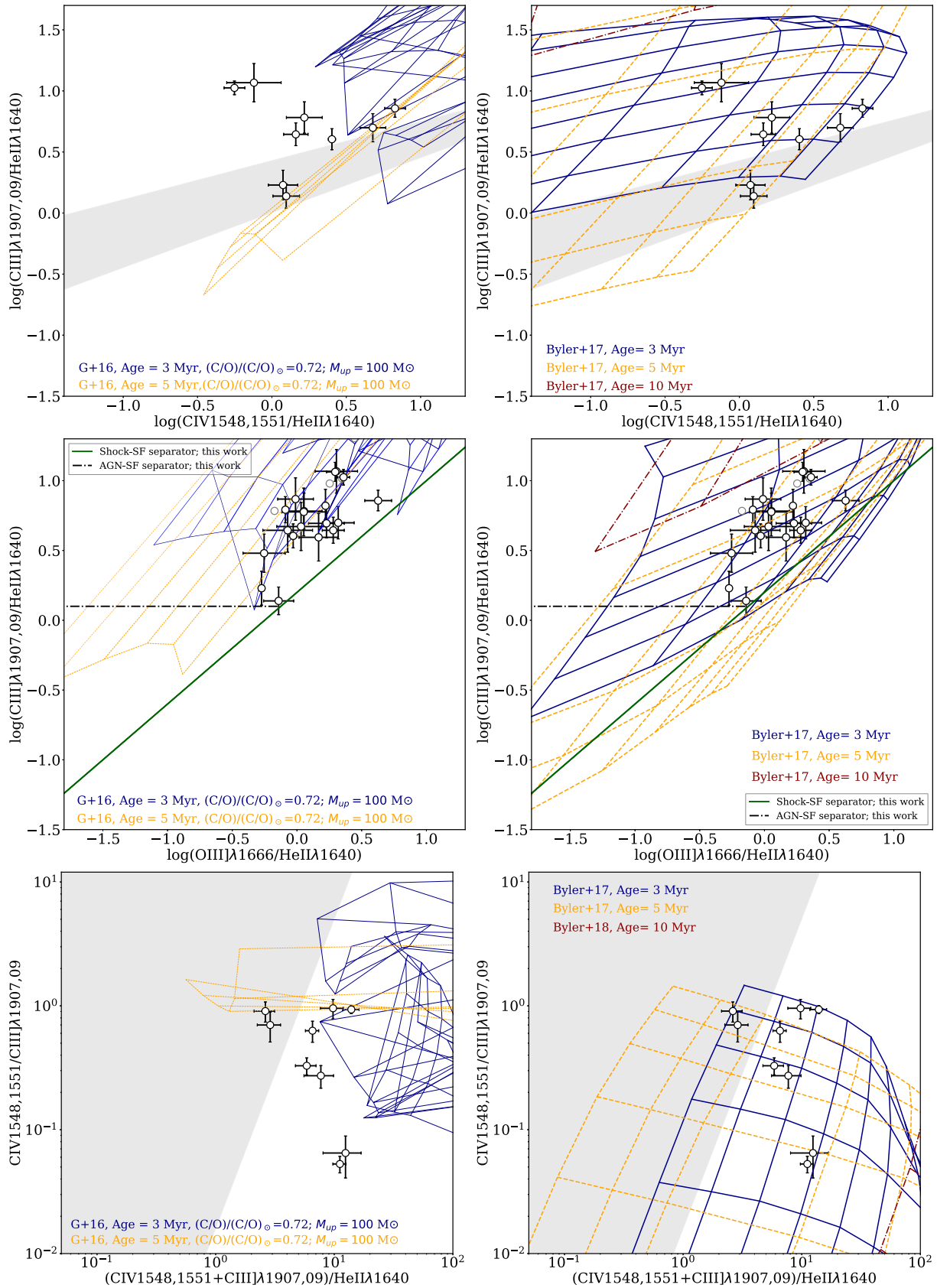

Figure 13. C3He2-C4He2, C3He2-C4C3, and C3He2-O3He2 diagrams as shown in Figures 5, 6, and 7 with overplotted G16 single-burst SF grids (left-hand panels) at 3 and 5 Myr in blue and orange, respectively, and B17 bursty models (right-hand panels) including stellar rotation at 3, 5, and 10 Myr in blue, orange, and red, respectively, as indicated in the legend. Lower C/O or higher IMF cut (not shown in the plot) has the effect of moving the 3 Myr G16 grids to lower C III]/He II and (C IV+C III])/He II line ratios, reproducing the observations, while at larger ages the stellar ionizing radiation is not enough. Indeed, stellar rotation and multiplicity (both not considered in G16) have the effect of amplifying the stellar ionizing radiation for several Myr after a SF burst.

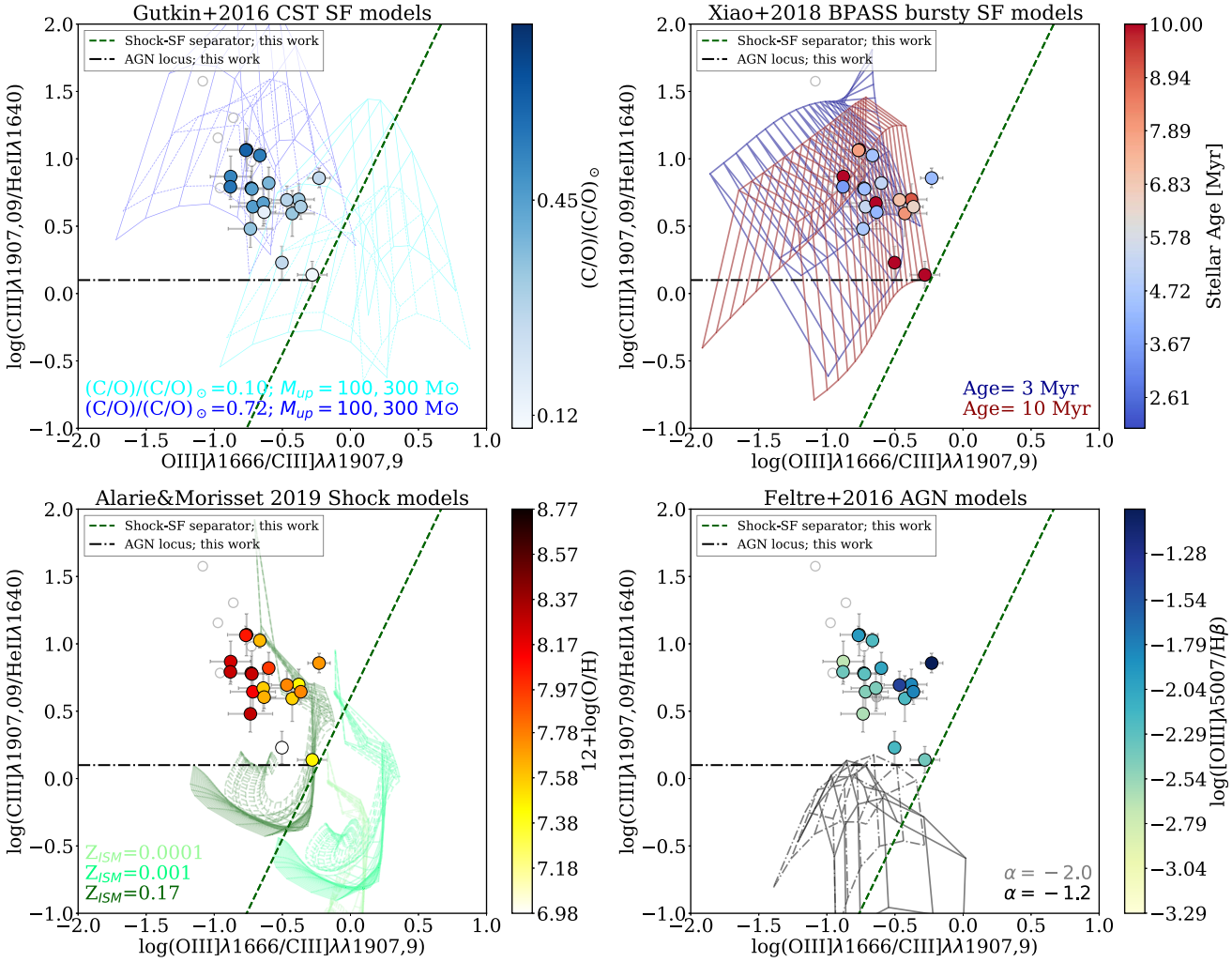

Figure 14. C3He2–O3C3 diagram: C III] $\lambda\lambda$1907,9/He II λ1640 vs O III] λ1666/C III] diagnostic plot proposed by F16 to separate SF and AGN activities. The filled and open dots show S/N > 3 and S/N < 3 fluxes for all the emission lines taken into account, respectively. The models superimposed are as explained in Figure 5. This diagram clearly distinguishes among SF, AGN, and shocks at subsolar metallicities (i.e., excluding the dark-green shock grid), as C3He2-O3He2 (Figure 6), as indicated by the dashed-dark-green and dashed–dotted-black lines.

shocks, as shown by the Shock-SF separator

$$y = 2.1\,x + 0.6 \tag{C1}$$

and the AGN-SF separator lines

$$y = 0.1 \quad \text{and} \quad x < -0.25 \tag{C2}$$

with $x = \log(\text{[O III]}\ \lambda1666/\text{C III]}\ \lambda\lambda1907,9)$ and $y = \log(\text{C III]}\ \lambda\lambda1907,9/\text{He II}\ \lambda1640)$. At subsolar metallicities (i.e., excluding the dark-green shock grid), shocks can reach higher [O III]/C III] line ratios than AGN models, while SF grids are located at higher C III]/He II values.

C3He2–C4C3 instead behaves similarly to C3He2–C4He2 diagram (Figure 5) and are a very similar version of the C4C3He2–C4C3 diagram (Figure 7). There is no clear difference in C IV/C III] line ratios between the different models, and thus the difference between SF and other mechanisms is mainly traced by the different C III]/He II (higher for SF grids, lower for AGN/shocks), as indicated by the Shock-SF separator

$$y \geqslant 0.1 \quad \text{and} \quad x \geqslant 0.1 \tag{C3}$$

and the AGN-SF separator lines

$$y = 0.1 \quad \text{and} \quad x < -0.25 \tag{C4}$$

with $x = \log(\text{C IV}\ \ \lambda\lambda1548,\ 51/\text{C III]}\ \lambda\lambda1907,9)$ and $y = \log(\text{C III]}\ \lambda\lambda1907,9/\text{He II}\ \lambda1640)$ In addition, AGN and shocks show similar C IV/C III], and thus this diagnostic diagram cannot distinguish them.

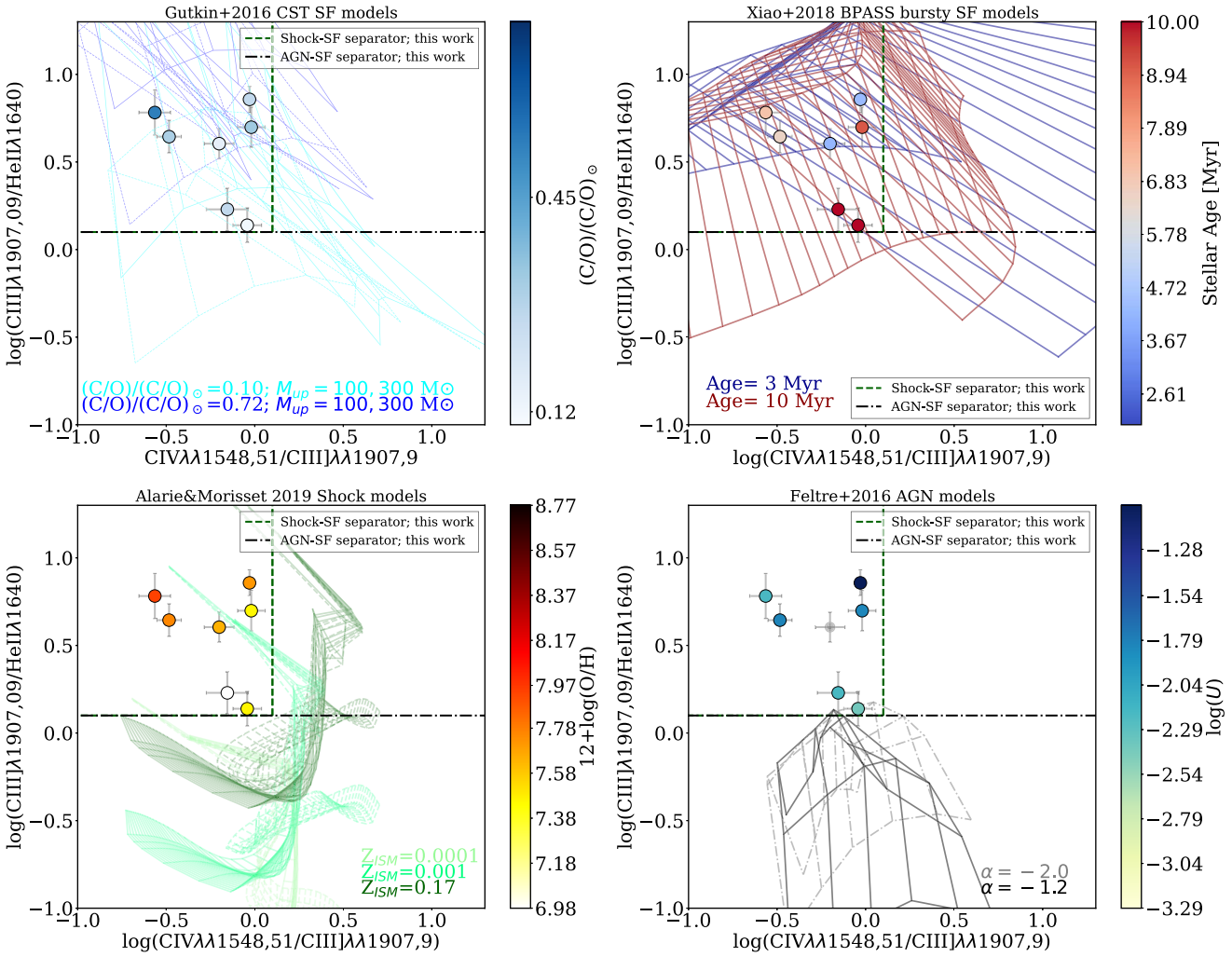

Figure 15. C3He2-C4C3 diagram: C III] λλ1907,9/He II λ1640 vs C IV λλ1548,51/C III] diagnostic plot proposed by F16 to separate SF and AGN activities. Here we show only the CLASSY galaxies with C IV detected in pure emission. The models that are superimposed are as explained in Figure 5. There is not a clear difference in C IV/C III] line ratios between the different models, and thus the difference between SF and other mechanisms is mainly traced by the different C III]/He II (higher for SF grids, lower for AGN/shocks), as indicated by the dashed-dark-green and dashed–dotted-black lines.

ORCID iDs

Matilde Mingozzi https://orcid.org/0000-0003-2589-762X
Bethan L. James https://orcid.org/0000-0003-4372-2006
Danielle A. Berg https://orcid.org/0000-0002-4153-053X
Karla Z. Arellano-Córdova https://orcid.org/0000-0002-2644-3518
Adele Plat https://orcid.org/0000-0003-0390-0656
Claudia Scarlata https://orcid.org/0000-0002-9136-8876
Alessandra Aloisi https://orcid.org/0000-0003-4137-882X
Ricardo O. Amorín https://orcid.org/0000-0001-5758-1000
Jarle Brinchmann https://orcid.org/0000-0003-4359-8797
Stéphane Charlot https://orcid.org/0000-0003-3458-2275
John Chisholm https://orcid.org/0000-0002-0302-2577
Anna Feltre https://orcid.org/0000-0001-6865-2871
Simon Gazagnes https://orcid.org/0000-0002-5659-4974
Matthew Hayes https://orcid.org/0000-0001-8587-218X
Timothy Heckman https://orcid.org/0000-0001-6670-6370
Svea Hernandez https://orcid.org/0000-0003-4857-8699
Lisa J. Kewley https://orcid.org/0000-0001-8152-3943
Nimisha Kumari https://orcid.org/0000-0002-5320-2568
Claus Leitherer https://orcid.org/0000-0003-2685-4488
Crystal L. Martin https://orcid.org/0000-0001-9189-7818
Michael Maseda https://orcid.org/0000-0003-0695-4414
Themiya Nanayakkara https://orcid.org/0000-0003-2804-0648
Swara Ravindranath https://orcid.org/0000-0002-5269-6527
Jane R. Rigby https://orcid.org/0000-0002-7627-6551
Peter Senchyna https://orcid.org/0000-0002-9132-6561
Evan D. Skillman https://orcid.org/0000-0003-0605-8732
Yuma Sugahara https://orcid.org/0000-0001-6958-7856
Stephen M. Wilkins https://orcid.org/0000-0003-3903-6935
Aida Wofford https://orcid.org/0000-0001-8289-3428
Xinfeng Xu https://orcid.org/0000-0002-9217-7051

References

Abazajian, K. N., Adelman-McCarthy, J. K., Agüeros, M. A., et al. 2009, ApJS, 182, 543
Alarie, A., & Morisset, C. 2019, RMxAA, 55, 377
Allen, M. G., Groves, B. A., Dopita, M. A., Sutherland, R. S., & Kewley, L. J. 2008, ApJS, 178, 20
Amorín, R., Vílchez, J. M., Hägele, G. F., et al. 2012, ApJL, 754, L22
Arellano-Córdova, K. Z., Berg, D. A., Chisholm, J., et al. 2022a, ApJL, 940, L23
Arellano-Córdova, K. Z., Mingozzi, M., Berg, D. A., et al. 2022b, ApJ, 935, 74

Arrabal Haro, P., Dickinson, M., Finkelstein, S. L., et al. 2023, ApJL, 951, L22
Asplund, M., Grevesse, N., Sauval, A. J., & Scott, P. 2009, ARA&A, 47, 481
Astropy Collaboration, Price-Whelan, A. M., Lim, P. L., et al. 2022, ApJ, 935, 167
Astropy Collaboration, Price-Whelan, A. M., Sipőcz, B. M., et al. 2018, AJ, 156, 123
Astropy Collaboration, Robitaille, T. P., Tollerud, E. J., et al. 2013, A&A, 558, A33
Atek, H., Labbé, I., Furtak, L. J., et al. 2023, arXiv:2308.08540
Bagley, M. B., Finkelstein, S. L., Koekemoer, A. M., et al. 2023, ApJL, 946, L12
Baldwin, J. A., Phillips, M. M., & Terlevich, R. 1981, PASP, 93, 5
Belfiore, F., Maiolino, R., Maraston, C., et al. 2016, MNRAS, 461, 3111
Berg, D. A., Chisholm, J., Erb, D. K., et al. 2019, ApJL, 878, L3
Berg, D. A., Chisholm, J., Erb, D. K., et al. 2021, ApJ, 922, 170
Berg, D. A., James, B. L., King, T., et al. 2022, ApJS, 261, 31
Berg, D. A., Skillman, E. D., Henry, R. B. C., Erb, D. K., & Carigi, L. 2016, ApJ, 827, 126
Bosch, G., Hägele, G. F., Amorín, R., et al. 2019, MNRAS, 489, 1787
Bradley, L., Sipőcz, B., Robitaille, T., et al. 2021, astropy/photutils: v1.1.0, Zenodo, doi:10.5281/zenodo.462499
Brinchmann, J., Kunth, D., & Durret, F. 2008, A&A, 485, 657
Bruzual, G., & Charlot, S. 2003, MNRAS, 344, 1000
Bundy, K., Bershady, M. A., Law, D. R., et al. 2015, ApJ, 798, 7
Bunker, A. J., Cameron, A. J., Curtis-Lake, E., et al. 2023a, arXiv:2306.02467
Bunker, A. J., Saxena, A., Cameron, A. J., et al. 2023b, A&A, 677, A88
Byler, N. 2018, nell-byler/cloudyfsps: Initial release of cloudyFSPS, v1.0.0, Zenodo, doi:10.5281/zenodo.1156412
Byler, N., Dalcanton, J. J., Conroy, C., et al. 2018, ApJ, 863, 14
Byler, N., Dalcanton, J. J., Conroy, C., & Johnson, B. D. 2017, ApJ, 840, 44
Byler, N., Kewley, L. J., Rigby, J. R., et al. 2020, ApJ, 893, 1
Cameron, A. J., Saxena, A., Bunker, A. J., et al. 2023, MNRAS, 523, 3516
Cann, J. M., Satyapal, S., Abel, N. P., et al. 2018, ApJ, 861, 142
Cann, J. M., Satyapal, S., Bohn, T., et al. 2020, ApJ, 895, 147
Cann, J. M., Satyapal, S., Rothberg, B., et al. 2021, ApJL, 912, L2
Cardelli, J. A., Clayton, G. C., & Mathis, J. S. 1989, ApJ, 345, 245
Castellano, M., Fontana, A., Treu, T., et al. 2022, ApJL, 938, L15
Chabrier, G. 2003, PASP, 115, 763
Charbonnel, C., Schaerer, D., Prantzos, N., et al. 2023, A&A, 673, L7
Chevallard, J., & Charlot, S. 2016, MNRAS, 462, 1415
Chisholm, J., Rigby, J. R., Bayliss, M., et al. 2019, ApJ, 882, 182
Concas, A., Maiolino, R., Curti, M., et al. 2022, MNRAS, 513, 2535
Crowther, P. A. 2007, ARA&A, 45, 177
Crowther, P. A., & Smith, L. J. 1997, A&A, 320, 500
Curti, M., D'Eugenio, F., Carniani, S., et al. 2022, MNRAS, 518, 425
Curti, M., Maiolino, R., Curtis-Lake, E., et al. 2023, arXiv:2304.08516
Curtis-Lake, E., Carniani, S., Cameron, A., et al. 2023, NatAs, 7, 622
del Valle-Espinosa, M. G., Sanchez-Janssen, R., Amorin, R., et al. 2023, MNRAS, 522, 2089
Denicoló, G., Terlevich, R., & Terlevich, E. 2002, MNRAS, 330, 69
Dopita, M. A., & Sutherland, R. S. 1995, ApJ, 455, 468
Dopita, M. A., & Sutherland, R. S. 1996, ApJS, 102, 161
Dopita, M. A., & Sutherland, R. S. 2003, Astrophysics of the Diffuse Universe (Berlin: Springer)
Dopita, M. A., Sutherland, R. S., Nicholls, D. C., Kewley, L. J., & Vogt, F. P. A. 2013, ApJS, 208, 10
Dors, O. L., Agarwal, B., Hägele, G. F., et al. 2018, MNRAS, 479, 2294
Draine, B. T. 2011, Physics of the Interstellar and Intergalactic Medium (Princeton, NJ: Princeton Univ. Press)
Du, X., Shapley, A. E., Martin, C. L., & Coil, A. L. 2017, ApJ, 838, 63
Eldridge, J. J., & Stanway, E. R. 2009, MNRAS, 400, 1019
Eldridge, J. J., Stanway, E. R., Xiao, L., & McClelland, L. A. S. 2017, PASA, 34, e058
Feltre, A., Charlot, S., & Gutkin, J. 2016, MNRAS, 456, 3354
Ferland, G. J., Porter, R. L., van Hoof, P. A. M., et al. 2013, RMxAA, 49, 137
Fernandes, I. F., Gruenwald, R., & Viegas, S. M. 2005, MNRAS, 364, 674
Finkelstein, S. L., Bagley, M. B., Arrabal Haro, P., et al. 2022, ApJL, 940, L55
Fosbury, R. A. E., Villar-Martín, M., Humphrey, A., et al. 2003, ApJ, 596, 797
Garnett, D. R., Kennicutt, R. C., Jr., Chu, Y. H., & Skillman, E. D. 1991, ApJ, 373, 458
Grandi, S. A. 1976, ApJ, 206, 658
Green, G. 2018, JOSS, 3, 695
Gronke, M., & Dijkstra, M. 2014, MNRAS, 444, 1095
Groves, B. A., Heckman, T. M., & Kauffmann, G. 2006, MNRAS, 371, 1559
Gutkin, J., Charlot, S., & Bruzual, G. 2016, MNRAS, 462, 1757
Harikane, Y., Nakajima, K., Ouchi, M., et al. 2024, ApJ, 960, 56
Hatano, S., Ouchi, M., Nakajima, K., et al. 2023, arXiv:2304.03726
Hayes, M. 2015, PASA, 32, e027
Heckman, T. M. 1980, A&A, 87, 152
Heckman, T. M., Robert, C., Leitherer, C., Garnett, D. R., & van der Rydt, F. 1998, ApJ, 503, 646
Henry, R. B. C., Edmunds, M. G., & Köppen, J. 2000, ApJ, 541, 660
Herenz, E. C., Micheva, G., Weilbacher, P. M., et al. 2023, RNAAS, 7, 99
Hirschmann, M., Charlot, S., Feltre, A., et al. 2019, MNRAS, 487, 333
Hirschmann, M., Charlot, S., Feltre, A., et al. 2023, MNRAS, 526, 3610
Ho, I. T., Kewley, L. J., Dopita, M. A., et al. 2014, MNRAS, 444, 3894
Hogarth, L., Amorín, R., Vílchez, J. M., et al. 2020, MNRAS, 494, 3541
Hu, W., Martin, C. L., Gronke, M., et al. 2023, ApJ, 956, 39
Izotov, Y. I., Chaffee, F. H., & Schaerer, D. 2001, A&A, 378, L45
Izotov, Y. I., Schaerer, D., Blecha, A., et al. 2006, A&A, 459, 71
Izotov, Y. I., & Thuan, T. X. 1999, ApJ, 511, 639
Izotov, Y. I., & Thuan, T. X. 2007, ApJ, 665, 1115
James, B. L., Berg, D. A., King, T., et al. 2022, ApJS, 262, 37
James, B. L., Pettini, M., Christensen, L., et al. 2014, MNRAS, 440, 1794
James, B. L., Tsamis, Y. G., Barlow, M. J., et al. 2009, MNRAS, 398, 2
Jaskot, A. E., & Ravindranath, S. 2016, ApJ, 833, 136
Kauffmann, G., Heckman, T. M., Tremonti, C., et al. 2003, MNRAS, 346, 1055
Keel, W. C. 1983, ApJ, 269, 466
Kelly, B. C. 2007, ApJ, 665, 1489
Kewley, L. J., & Dopita, M. A. 2002, ApJS, 142, 35
Kewley, L. J., Dopita, M. A., Sutherland, R. S., Heisler, C. A., & Trevena, J. 2001, ApJ, 556, 121
Kewley, L. J., & Ellison, S. L. 2008, ApJ, 681, 1183
Kewley, L. J., Groves, B., Kauffmann, G., & Heckman, T. 2006, MNRAS, 372, 961
Kewley, L. J., Nicholls, D. C., & Sutherland, R. S. 2019, ARA&A, 57, 511
Kluyver, T., Ragan-Kelley, B., Pérez, F., et al. 2016, in Positioning and Power in Academic Publishing: Players, Agents and Agendas, ed. F. Loizides & B. Schmidt (Amsterdam: IOS Press), 87
Komarova, L., Oey, M. S., Krumholz, M. R., et al. 2021, ApJL, 920, L46
Korista, K. T., & Ferland, G. J. 1989, ApJ, 343, 678
Kroupa, P. 2001, MNRAS, 322, 231
Lamareille, F. 2010, A&A, 509, A53
Lamareille, F., Mouhcine, M., Contini, T., Lewis, I., & Maddox, S. 2004, MNRAS, 350, 396
Leitherer, C., Leão, J. R. S., Heckman, T. M., et al. 2001, ApJ, 550, 724
Luridiana, V., Morisset, C., & Shaw, R. A. 2012, in IAU Symp. 283, Planetary Nebulae: An Eye to the Future, ed. A. Manchado, L. Stanghellini, & D. Schönberner (Cambridge: Cambridge Univ. Press), 422
Luridiana, V., Morisset, C., & Shaw, R. A. 2015, A&A, 573, A42
Madau, P., & Haardt, F. 2015, ApJL, 813, L8
Mainali, R., Kollmeier, J. A., Stark, D. P., et al. 2017, ApJL, 836, L14
Mainali, R., Zitrin, A., Stark, D. P., et al. 2018, MNRAS, 479, 1180
Maiolino, R., Scholtz, J., Witstok, J., et al. 2023, arXiv:2305.12492
Marasco, A., Belfiore, F., Cresci, G., et al. 2023, A&A, 670, A92
Markwardt, C. B. 2009, in ASP Conf. Ser. 411, Astronomical Data Analysis Software and Systems XVIII, ed. D. A. Bohlender, D. Durand, & P. Dowler (San Francisco, CA: ASP), 251
Maseda, M. V., Brinchmann, J., Franx, M., et al. 2017, A&A, 608, A4
Matthee, J., Mackenzie, R., Simcoe, R. A., et al. 2023, ApJ, 950, 67
Mayya, Y. D., Plat, A., Gómez-González, V. M. A., et al. 2023, MNRAS, 519, 5492
McElroy, R., Croom, S. M., Pracy, M., et al. 2015, MNRAS, 446, 2186
Michel-Dansac, L., Blaizot, J., Garel, T., et al. 2020, A&A, 635, A154
Mingozzi, M., Cresci, G., Venturi, G., et al. 2019, A&A, 622, A146
Mingozzi, M., James, B. L., Arellano-Córdova, K. Z., et al. 2022, ApJ, 939, 110
Molina, M., Reines, A. E., Latimer, L. J., Baldassare, V., & Salehirad, S. 2021, ApJ, 922, 155
Nagao, T., Maiolino, R., & Marconi, A. 2006, A&A, 447, 863
Nakajima, K., & Maiolino, R. 2022, MNRAS, 513, 5134
Nakajima, K., Schaerer, D., Le Fèvre, O., et al. 2018, A&A, 612, A94
Nanayakkara, T., Brinchmann, J., Boogaard, L., et al. 2019, A&A, 624, A89
Osterbrock, D. E., & Ferland, G. J. 2006, Astrophysics of Gaseous Nebulae and Active Galactic Nuclei (Sausalito, CA: Univ. Science Books)
Pascale, M., Dai, L., McKee, C. F., & Tsang, B. T. H. 2023, ApJ, 957, 77
Pettini, M., & Pagel, B. E. J. 2004, MNRAS, 348, L59
Plat, A., Charlot, S., Bruzual, G., et al. 2019, MNRAS, 490, 978
Polimera, M. S., Kannappan, S. J., Richardson, C. T., et al. 2022, ApJ, 931, 44
Raiter, A., Fosbury, R. A. E., & Teimoorinia, H. 2010, A&A, 510, A109

Ravindranath, S., Monroe, T., Jaskot, A., Ferguson, H. C., & Tumlinson, J. 2020, ApJ, 896, 170
Reines, A. E., Condon, J. J., Darling, J., & Greene, J. E. 2020, ApJ, 888, 36
Rich, J. A., Dopita, M. A., Kewley, L. J., & Rupke, D. S. N. 2010, ApJ, 721, 505
Rigby, J. R., Bayliss, M. B., & Gladders, M. D. 2015, ApJL, 814, L6
Rigby, J. R., Bayliss, M. B., Sharon, K., et al. 2018, AJ, 155, 104
Roberts-Borsani, G., Morishita, T., Treu, T., et al. 2022, ApJL, 938, L13
Robertson, B. E., Ellis, R. S., Furlanetto, S. R., & Dunlop, J. S. 2015, ApJL, 802, L19
Sartori, L. F., Schawinski, K., Treister, E., et al. 2015, MNRAS, 454, 3722
Scarlata, C., & Panagia, N. 2015, ApJ, 801, 43
Schaerer, D., Izotov, Y. I., Worseck, G., et al. 2022, A&A, 658, L11
Schaerer, D., & Vacca, W. D. 1998, ApJ, 497, 618
Schmutz, W., Leitherer, C., & Gruenwald, R. 1992, PASP, 104, 1164
Senchyna, P., Plat, A., Stark, D. P., & Rudie, G. C. 2023b, arXiv:2303.04179
Senchyna, P., Stark, D. P., Charlot, S., et al. 2021, MNRAS, 503, 6122
Senchyna, P., Stark, D. P., Chevallard, J., et al. 2019, MNRAS, 488, 3492
Shapley, A. E., Steidel, C. C., Pettini, M., & Adelberger, K. L. 2003, ApJ, 588, 65
Shirazi, M., & Brinchmann, J. 2012, MNRAS, 421, 1043
Simmonds, C., Tacchella, S., Hainline, K., et al. 2024, MNRAS, 527, 6139
Sixtos, A., Wofford, A., Sander, A. A. C., & Peimbert, A. 2023, MNRAS, 519, 5656
Smith, L. J., Oey, M. S., Hernandez, S., et al. 2023, ApJ, 958, 194
Stanway, E. R., Eldridge, J. J., & Becker, G. D. 2016, MNRAS, 456, 485
Stark, D. P. 2016, ARA&A, 54, 761
Stark, D. P., Richard, J., & Charlot, S. 2015, MNRAS, 450, 1846
Stasińska, G., Izotov, Y., Morisset, C., & Guseva, N. 2015, A&A, 576, A83
Steidel, C. C., Strom, A. L., Pettini, M., et al. 2016, ApJ, 826, 159
Stephenson, M. G., Arellano-Córdova, K. Z., Berg, D. A., Mingozzi, M., & James, B. L. 2023, RNAAS, 7, 31
Sutherland, R. S., & Dopita, M. A. 2017, ApJS, 229, 34
Thuan, T. X., & Izotov, Y. I. 2005, ApJS, 161, 240
Tozzi, G., Maiolino, R., Cresci, G., et al. 2023, MNRAS, 521, 1264
Treu, T., Roberts-Borsani, G., Bradac, M., et al. 2022, ApJ, 935, 110
Trump, J. R., Arrabal Haro, P., Simons, R. C., et al. 2023, ApJ, 945, 35
Vanzella, E., Grazian, A., Hayes, M., et al. 2010, A&A, 513, A20
Veilleux, S., & Osterbrock, D. E. 1987, ApJS, 63, 295
Verhamme, A., Orlitová, I., Schaerer, D., et al. 2017, A&A, 597, A13
Wise, J. H., Demchenko, V. G., Halicek, M. T., et al. 2014, MNRAS, 442, 2560
Wofford, A., Sixtos, A., Charlot, S., et al. 2023, MNRAS, 523, 3949
Wofford, A., Vidal-García, A., Feltre, A., Chevallard, J., et al. 2021, MNRAS, 500, 2908
Xiao, L., Stanway, E. R., & Eldridge, J. J. 2018, MNRAS, 477, 904
Xu, X., Heckman, T., Henry, A., et al. 2022, ApJ, 933, 222
Xu, X., Heckman, T., Henry, A., et al. 2023, ApJ, 948, 28